The Balloon-borne Large Aperture Submillimeter Telescope (BLAST) 2005: A 4 deg^2 Galactic Plane Survey in Vulpecula ($\ell = 59°$)

E. L. Chapin,[1,†] P. A. R. Ade,[2] J. J. Bock,[3,4] C. Brunt,[5] M. J. Devlin,[6] S. Dicker,[6] M. Griffin,[2] J. O. Gundersen,[7] M. Halpern,[1] P. C. Hargrave,[2] D. H. Hughes,[8] J. Klein,[6] G. Marsden,[1] P. G. Martin,[9,10] P. Mauskopf,[2] C. B. Netterfield,[10,11] L. Olmi,[12,13] E. Pascale,[11] G. Patanchon,[1,14] M. Rex,[6] D. Scott,[1] C. Semisch,[6] M. D. P. Truch,[15] C. Tucker,[2] G. S. Tucker,[15] M. P. Viero,[10] D. V. Wiebe[11]

ABSTRACT

We present the first results from a new 250, 350, and 500 μm Galactic Plane survey taken with the Balloon-borne Large-Aperture Submillimeter Telescope (BLAST) in 2005. This survey's primary goal is to identify and characterize high-mass proto-stellar objects (HMPOs). The region studied here covers 4 deg^2 near the open cluster NGC 6823 in the constellation Vulpecula ($\ell = 59°$). We find 60 compact sources ($< 60''$ diameter) detected simultaneously in all three bands. Their spectral energy distributions (SEDs) are constrained through BLAST, *IRAS*, *Spitzer* MIPS, and *MSX* photometry, with inferred dust temperatures spanning ~ 12–40 K assuming a dust emissivity index $\beta = 1.5$. The luminosity-to-mass ratio, a distance-independent quantity, spans ~ 0.2–130 $L_\odot\,M_\odot^{-1}$. Distances are estimated from coincident ^{13}CO$(1 \rightarrow 0)$ velocities combined with a variety of other velocity and morphological data in the literature. In total, 49 sources are associated with a molecular cloud complex encompassing NGC 6823 (distance ~ 2.3 kpc), 10 objects with the Perseus Arm (~ 8.5 kpc) and one object is probably in the outer Galaxy (~ 14 kpc). Near NGC 6823, the inferred luminosities and masses of BLAST sources span ~ 40–$10^4\,L_\odot$, and ~ 15–700 $M_\odot$, respectively. The mass spectrum is compatible with molecular gas masses in other high-mass star forming regions. Several luminous sources appear to be Ultra

[1]Department of Physics & Astronomy, University of British Columbia, 6224 Agricultural Road, Vancouver, BC V6T 1Z1, Canada

[2]Department of Physics & Astronomy, Cardiff University, 5 The Parade, Cardiff, CF24 3AA, UK

[3]Jet Propulsion Laboratory, Pasadena, CA 91109-8099

[4]Observational Cosmology, MS 59-33, California Institute of Technology, Pasadena, CA 91125

[5]School of Physics, University of Exeter, Stocker Road, Exeter, EX4 4QL, UK

[6]Department of Physics and Astronomy, University of Pennsylvania, 209 South 33rd Street, Philadelphia, PA 19104

[7]Department of Physics, University of Miami, 1320 Campo Sano Drive, Carol Gables, FL 33146

[8]Instituto Nacional de Astrofísica Óptica y Electrónica (INAOE), Aptdo. Postal 51 y 72000 Puebla, Mexico

[9]Canadian Institute for Theoretical Astrophysics, University of Toronto, 60 St. George Street, Toronto, ON M5S 3H8, Canada

[10]Department of Astronomy & Astrophysics, University of Toronto, 50 St. George Street, Toronto, ON M5S 3H4, Canada

[11]Department of Physics, University of Toronto, 60 St. George Street, Toronto, ON M5S 1A7, Canada

[12]Istituto di Radioastronomia, Largo E. Fermi 5, I-50125, Firenze, Italy

[13]University of Puerto Rico, Rio Piedras Campus, Physics Dept., Box 23343, UPR station, San Juan, Puerto Rico

[14]Laboratoire APC, 10, rue Alice Domon et Léonie Duquet 75205 Paris, France

[15]Department of Physics, Brown University, 182 Hope Street, Providence, RI 02912

[†]echapin@phas.ubc.ca

Compact H II regions powered by early B stars. However, many of the objects are cool, massive gravitationally-bound clumps with no obvious internal radiation from a protostar, and hence excellent HMPO candidates.

Subject headings: submillimeter — stars: formation — ISM: clouds — balloons

1. INTRODUCTION

The Balloon-borne Large Aperture Submillimeter Telescope (BLAST) is a 2-m stratospheric balloon telescope that observes simultaneously at 250, 350, and $500\,\mu$m using bolometric imaging arrays (Pascale et al. 2007). During the first BLAST science flight, a 100 hr Arctic flight from Sweden to Canada in June 2005 (BLAST05), BLAST conducted the first sensitive large-scale Galactic Plane surveys at these wavelengths. The focus of these surveys is the earliest stages of massive star formation. As noted in the recent review by Zinnecker & Yorke (2007) our understanding of this evolutionary phase is still limited. Over the past 15 years submillimeter observations at longer wavelengths (350–$1200\,\mu$m), e.g. with SCUBA on the 15-m James Clerk Maxwell Telescope (Holland et al. 1999), or MAMBO on the IRAM 30-m telescope (Kreysa et al. 1998; Motte et al. 2007), have opened up studies of the earliest evolutionary stages of molecular core collapse and proto-stellar formation. Such cores lack an internal source of radiation and are very cold ($\lesssim 25\,$K), so that they emit the bulk of their radiation at submillimeter wavelengths. Since this emission is optically thin in the submillimeter band, observed flux densities are proportional to column density and mass. There is a variety of terminology used for these elusive early stages. For example, Zinnecker & Yorke (2007) distinguish cores (size $0.1\,$pc) embedded within clumps (size $0.5\,$pc). Motte et al. (2007) refer to molecular cloud fragments which could be high-luminosity infra-red protostars, infra-red quiet protostars, or high-mass pre-stellar cores. Along the lines of the latter, here we refer to high-mass proto-stellar objects (HMPOs) as compact sources residing in dense molecular clouds, that have the potential to form (one or more) massive OB stars, having luminosities in the range $\sim 10^2$–$10^5\,$L$_\odot$, but without associated radio continuum emission. This latter qualification distinguishes them from massive young stellar objects, a later stage in which a hot star has formed (perhaps still accreting), providing the ionizing radiation necessary to form a high

emission measure Ultra Compact (UC) H II region (and hence radio emission). Note that at the distances of high-mass star forming regions surveying instruments detect quite massive clumps, possibly harboring groups of stars or their precursors, and not resolving the substructure associated with individual nodes of collapse; however, once star formation is underway the most massive objects dominate the luminosity and ionization.

BLAST is presently unique in its ability to detect and characterize cold dust emission from a range of pre- and proto-stellar sources, constraining the temperatures of objects with $T \lesssim 25\,$K ($\beta = 1.5$) using its three-band photometry near the peak of the spectrum. An earlier, less sensitive balloon-borne submillimeter telescope called ProNaOS (Dupac et al. 2001) had similar goals. Previous studies which do not sample the spectral peak of the thermal emission (e.g., Johnstone et al. 2000; Pierce-Price et al. 2000; Kirk et al. 2005; Reid & Wilson 2005; Thompson et al. 2005; Enoch et al. 2006; Hill et al. 2006; Schneider et al. 2006; Thompson et al. 2006; Young et al. 2006; Enoch et al. 2007; Moore et al. 2007) have been limited by their relative inability to measure the temperature, producing large uncertainties in the derived luminosities and masses. Recent surveys with *Spitzer* MIPS can constrain the temperatures of warmer objects (Carey et al. 2005), but the youngest and coldest objects are potentially not detected even in the long-wavelength *Spitzer* bands.

BLAST is also very efficient at mapping, and so conducted a series of surveys spread across the entire portion of the Galactic Plane that was available during the flight. These maps encompass (primarily) known high-mass star forming regions: a $10\,$deg^2 map of Cygnus X; a $4\,$deg^2 map in Vulpecula (described in detail in this paper); a $3\,$deg^2 map in Sagitta; and finally a $6\,$deg^2 map in Aquila towards the Galactic Ring Survey molecular cloud GRSMC 45.60+0.30 (Rathborne et al. 2004). The locations and sizes of these maps are shown in Figure 1. The Vulpecula map was stud-

ied first, as it is the deepest of the four regions, and consists of 6.5 hours of data. The analysis of the other three fields, and those from the 2006 Antarctic flight, including a diffraction-limited $50 \deg^2$ map of the Vela molecular ridge, will be presented in forthcoming papers.

To put these surveys in context, Motte et al. (2007) state that "large fast-mapping images with MAMBO-2 are currently the best tool to study density structure of molecular clouds with high spatial resolution." In about 33 hours of observations (and 30 more with the less efficient MAMBO) they mapped $3 \deg^2$ in Cygnus X; not the entire region but targeted areas of high extinction. They catalogued 129 compact sources (down to a scale of $15''$) to a peak flux level of $80 \, \mathrm{mJy}$ ($5 \, \sigma$) and proposed an additional 40 somewhat more extended structures ($2'$). Larger structures ($10'$) were filtered out. In the survey reported here, we mapped a contiguous (no threshold for extinction) $4 \deg^2$ in 6.5 hours. Although the very largest scales (including the DC level) are absent from our maps, our images maintain power well beyond $10'$; the images reveal interesting large-scale structures crossing the entire region. As reported below, we catalog 60 sources to a flux level of $10 \, \mathrm{Jy}$ at $250 \, \mu\mathrm{m}$. Extrapolating this detection limit using a typical spectral shape ($T = 20 \, \mathrm{K}$ and $\beta = 1.5$) this corresponds to $170 \, \mathrm{mJy}$ at $1.2 \, \mathrm{mm}$. We also find fewer sources per square degree compared to the Motte et al. (2007) survey of Cygnus X because this region is slightly more distant, not as active, and our survey did not target areas of high extinction. There are exciting large sensitive surveys to look forward to at these same wavelengths with the SPIRE instrument for *Herschel* (Griffin et al. 2003).

The region chosen for this study was centered near NGC 6823 in the constellation Vulpecula ($\ell = 59°$), and covers approximately $4 \deg^2$. This region of the Galactic Plane is prominent in images of thermal dust emission (e.g., *IRAS* in Figure 1), as well as in the radio and the optical. In the radio, the identifiable extended H II region excited by the massive stars is called Sh2-86 (nominal position indicated in Figure 2). The stellar HR diagram for NGC 6823 has been examined by Massey et al. (1995). They find an age of 5–7 Myr for the bulk of the stars. There are several evolved OB supergiants of mass $\sim 25 \, \mathrm{M_\odot}$. The most massive star, O7 V ((f)), with mass $\sim 40 \, \mathrm{M_\odot}$, appears younger ($2 \, \mathrm{Myr}$) than the rest. In the optical this massive star is responsible for the illumination of many "elephant trunks" or "pillars" in the eastern portion of the H II region.

Very high-mass stars evolve quickly into supernovae. We note that a supernova remnant (SNR) discovered by Taylor et al. (1992) is within $20'$ of the O7 star in projection ($< 12 \, \mathrm{pc}$ laterally, assuming the same distance), and even closer to one B supergiant — nominal positions are indicated in Figure 2. Massey et al. (1995) find several pre-main sequence stars of mass 5–$7 \, \mathrm{M_\odot}$, which pass through this stage in less than $2 \, \mathrm{Myr}$. Earlier stages of evolution are revealed by the bright Infra Red Astronomy Satellite (*IRAS*) sources clustered in this region. At least seven of these objects have been observed in molecular line studies (Beuther et al. 2002; Zhang et al. 2005; Beltrán et al. 2006)

This paper describes a technique developed for deconvolving the out-of-focus beams common to all data from BLAST05 (see Truch et al. 2007) and for detecting compact objects in the BLAST maps. We report a robust list of 60 submillimeter sources with sizes $\lesssim 60''$ diameter that are detected simultaneously in the three BLAST bands (§2). Infra-red photometry for BLAST sources is obtained from comparisons with *IRAS* and *Spitzer* MIPS maps, and the Midcourse Space Experiment (*MSX*) point source catalog (§3). The BLAST and infra-red data are combined to constrain dust temperatures and integrated far infra-red (FIR) fluxes using isothermal modified blackbody SED fits (§4). Our analysis has benefited from a $^{13}\mathrm{CO}(1 \to 0)$ data cube obtained as a part of a Galactic Plane survey at FCRAO (Brunt & Heyer 2007). Noting coincidences between compact structures in the $^{13}\mathrm{CO}$ emission, and comparing velocities and morphologies with the VLA Galactic Plane Survey, *Spitzer* GLIMPSE (Whitney & GLIMPSE Team 2005) and Digitized Sky Survey images, distance estimates are obtained for all of the sources in §5. Of 60 BLAST sources, 49 objects are likely associated with the molecular clouds surrounding NGC 6823 at $\sim 2.3 \, \mathrm{kpc}$, 10 appear to be in the more distant Perseus arm ($\sim 8.5 \, \mathrm{kpc}$), and a single object is thought to lie in the outer Galaxy ($\sim 14 \, \mathrm{kpc}$). These distances are used to calculate source lu-
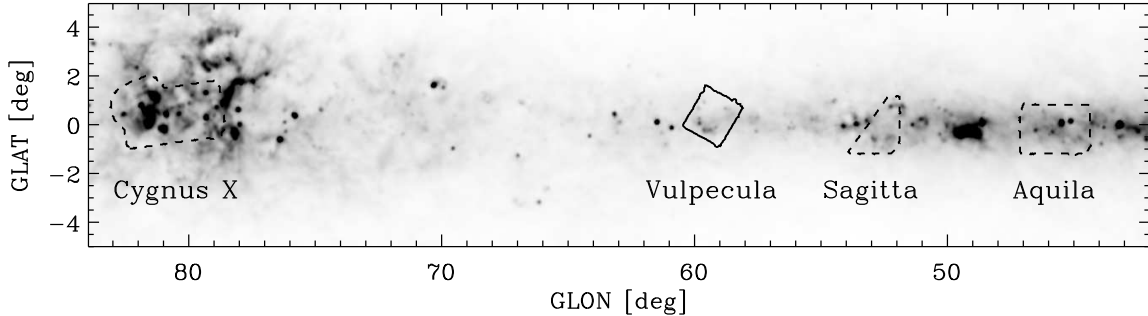
Fig. 1.— Locations of fields for the BLAST05 Galactic Plane surveys. Results from the Vulpecula field are discussed in detail in this paper. The background intensity image is $100\,\mu$m emission from Schlegel et al. (1998).

minosities and masses in §6. In this section we also present an estimate of the mass function for sources associated with NGC 6823. In this survey high-mass clumps are seen in a range of evolutionary stages: those with embedded UC H II regions; luminous objects without substantial radio emission (HMPOs); and cold gravitationally-bound clumps (or cores) with low luminosity-to-mass ratio and no evidence of star formation (§7).

2. BLAST OBSERVATIONS TOWARDS NGC 6823

2.1. Observing Strategy

BLAST05 is a 2-m Cassegrain telescope, whose under-illuminated primary mirror is designed to produce diffraction-limited beams with FWHM $40''$, $58''$, and $75''$ at 250, 350, and $500\,\mu$m respectively. The camera consists of three silicon-nitride "spider web" bolometer arrays (Turner et al. 2001) almost identical to those for SPIRE on *Herschel* (Griffin et al. 2003), with 149, 88, and 43 detectors at 250, 350, and $500\,\mu$m, organized in a hexagonal close-packed pattern. Radiation is coupled to the bolometers using $2f\lambda$ spaced conical feed-horns, so that the $14' \times 7'$ field-of-view (simultaneously imaged by all three arrays) is instantaneously under-sampled. The telescope must therefore scan in order to produce fully-sampled images. Scanning is also required to modulate the bolometer signals to remove low-frequency detector drift. A full description of the BLAST telescope and detectors is given in Pascale et al. (2007). The 2005 Sweden flight performance is described in Truch et al. (2007).

The optimal detector noise was obtained by scanning the telescope in azimuth at $0.1\deg\mathrm{s}^{-1}$ while drifting slowly in elevation such that the scan lines are spaced $65''$ apart. In addition, observations of Vulpecula were split between times when it was rising and setting, resulting in cross-linked scans at angles of $\sim 45°$. This cross-linking greatly reduces large-scale $1/f$ noise in the map. Details of the BLAST scanning technique are given in Pascale et al. (2007).

2.2. Data Reduction

The raw BLAST05 data are reduced using a common pipeline detailed in Pascale et al. (2007) and Truch et al. (2007). First, the 100 Hz sampled bolometer and gondola pointing data are de-spiked and the digital filter responses are deconvolved. Time-varying bolometer responsivities are tracked using an internal calibration lamp. The absolute gain of the instrument (including antenna efficiency), determined from regular observations of Arp 220, is measured with absolute uncertainties of 8%, 10%, and 12% at 500, 350, and $250\,\mu$m respectively. The relative pointing of the telescope within a single map is determined to $< 5''$ rms by integrating rate gyroscopes with star trackers providing an absolute reference. Residual pointing offsets between different observations of Vulpecula are removed by direct rebinning of the data into maps, and aligning the peaks of the seven brightest compact sources from each pass. Finally, maps are made using a new algorithm called Signal And Noise Estimation Procedure Including Cor-

4

relations (SANEPIC). This technique has evolved from strategies used to produce maps of the Cosmic Microwave Background. A model is first developed for the raw bolometer time-stream data in which the astronomical signal is produced by projecting the estimate of the map into the time domain using the known positions of each detector over time, and assuming that the noise is Gaussian, stationary, and correlated in time and between detectors. The brightness of each map pixel is considered a free parameter in this model. A maximum likelihood solution for the map is then found using a direct inversion technique. This calculation includes the full noise power spectra of the bolometers, and propagates knowledge of correlations in the bolometer data to pixels in the map. Low-frequency noise (predominantly slowly-varying sky emission) is naturally removed by this process. In particular, to reconstruct large spatial scales in the map, this method gives more weight to data taken during a single visit, during which the bolometer zero-point drift is minimal. The DC level of the map is unconstrained, and set to 0 by applying a weak high-pass filter to the bolometer data before map-making. The details of SANEPIC are given in Patanchon et al. (2007).

2.3. Overview of the Maps

The BLAST05 maps of Vulpecula are shown in Figure 2. The similarity of the three maps is striking, both in the diffuse emission and the peaks, demonstrating that the bulk of the measurements fall on the Rayleigh-Jeans tail of the thermal emission. In this case, they are a good measure of dust column density in the molecular cloud and the mass of the compact sources.

The far-infrared (60 and $100\,\mu$m) emission in this part of Vulpecula is dominated by several luminous high-mass star forming regions. Three of these have been studied recently by Beltrán et al. (2006) and Zhang et al. (2005), associated with the following IRAS sources (for later cross-reference we append the BLAST name from Table 3): 19368+2239 (V03); 19374+2352 (V05); and 19388+2357 (V08). A further four regions have been studied extensively by Beuther et al. (2002), using CS multi-line, multi-isotopolog observations and the 1.2 mm dust continuum: 19403+2258 (V18); 19410+2336 (V30); 19411+2306 (V32); and 19413+2332 (V40). Note that these
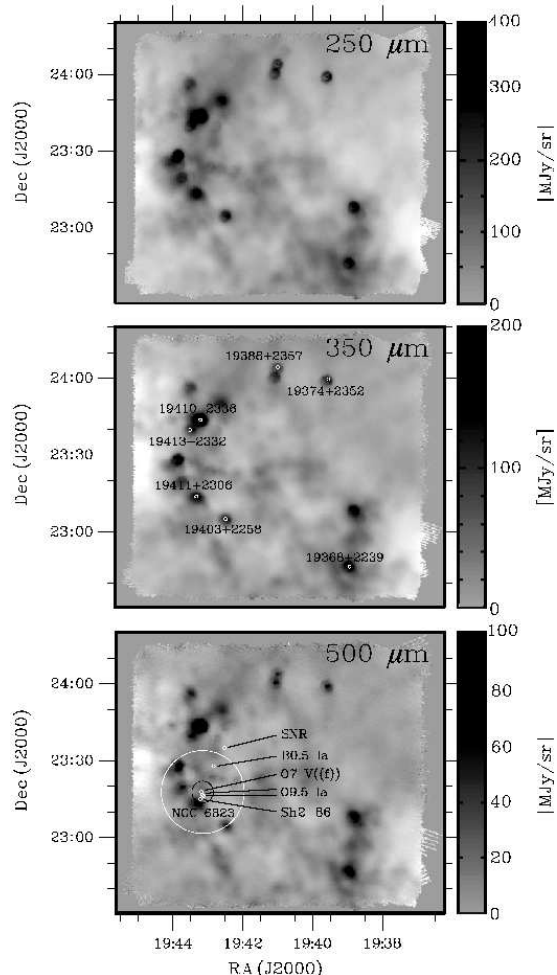

Fig. 2.— Raw BLAST05 maps of Vulpecula produced with SANEPIC (Patanchon et al. 2007). The similarity between the bands is due to the filters sampling primarily the Rayleigh-Jeans spectrum of thermal dust emission. Previously identified *IRAS* sources associated with high-mass star forming regions are indicated on the $350\,\mu$m map (see §2.3). It is assumed that most of the submillimeter emission originates in a molecular cloud complex at the distance of the open cluster NGC 6823 (~ 2.3 kpc away) indicated in the $500\,\mu$m map (the two circles give the cluster core size, and maximum extents, respectively). The locations of several OB supergiants, an O7 V ((f)) star, and a supernova remnant, all associated with NGC 6823, are also shown. Sh2-86 is an extended H II region excited by these massive stars.

TABLE 1

VULPECULA MAP SENSITIVITIES.

Band (μm)	FWHP ($''$)	σ_b ($''$)	σ_p (mJy)	σ_s (Jy)
Raw maps				
250	207	88.2	18.0	0.32
350	206	87.8	9.9	0.17
500	212	90.4	9.9	0.18
Deconvolved maps				
250	40	17.0	350.0	1.17
350	50	21.3	99.0	0.41
500	60	25.5	122.0	0.61

NOTE.—Full-Width Half-Power (FWHP) is the diameter in which 50% of the beam power is contained (equivalent to Full-Width Half-Maximum for Gaussian beams). The standard deviation (size) of a Gaussian beam with the equivalent FWHP is given by σ_b. The rms noise in a single 18$''$ map pixel is given by σ_p. The rms noise in the equivalent FWHP Gaussian beam is given by σ_s. Values are presented both for "Raw maps" produced with SANEPIC (§2.3) and for "Deconvolved maps" (§2.4).

do not exhaust the list of bright sources, either at submillimeter or far-infrared wavelengths.

In the submillimeter, the brightest high-mass star forming region near IRAS 19410+2336 is visible in the north-east part of the BLAST maps (Figure 2). The other bright regions are located on a roughly "C"-shaped arc readily apparent in the *IRAS* maps. As with *IRAS*, the BLAST emission is in most cases centrally peaked, representing a single massive clump at the observed resolution of BLAST. There is also diffuse emission from extended clouds of dust, as well as blending of (clustered) point sources convolved with the beam.

In the 2005 flight, the point spread function (PSF) was not diffraction-limited ($40''$, $58''$, and $75''$ at 250, 350, and $500\,\mu m$ respectively) as originally designed. The resulting full-width half-powers (FWHP, equivalent to the full-width half-maximum for a Gaussian) in all three bands are approximately $3'\!.5$ and exhibit complex shapes that vary as a function of wavelength and position in the focal plane (Truch et al. 2007).

The beam shape is clearly recognizable at many locations across the entire field, suggesting the presence of point-like objects with angular scales smaller than the beam. However, the overlapping beam patterns also indicate that the maps are highly source-confused (Figure 2). Even though only 3–8% of the beam power is found in the central diffraction-limited peak at each wavelength, the signal-to-noise (S/N) of the maps are high enough (compare sensitivity for "Raw maps" in Table 1 with typical source flux densities in later tables) that we are able to deconvolve a significant fraction of the beam to recover angular scales close to the diffraction limit. We can then use these deconvolved maps to search for compact sources.

2.4. Image Deconvolution

Deconvolution in astronomy has a long history (see the review by Starck et al. 2002). The convolution problem can be stated, using the notation of Starck et al. (2002), as

$$I(x,y) = (O * P)(x,y) + N(x,y), \qquad (1)$$

where I is the observed map, O is the true image, P is the instrument's PSF, N is measurement noise, and "$*$" is the convolution operator. Invoking the convolution theorem, this expression can

be written in Fourier space as

$$\hat{I}(u,v) = \hat{O}(u,v)\hat{P}(u,v) + \hat{N}(u,v), \qquad (2)$$

where $\hat{X}$ is the Fourier transform of X. A naive solution to the convolution problem is found by simple division in Fourier space,

$$\hat{\tilde{O}}(u,v) = \frac{\hat{I}(u,v)}{\hat{P}(u,v)} = \hat{O}(u,v) + \frac{\hat{N}(u,v)}{\hat{P}(u,v)}. \qquad (3)$$

However, in practice, this direct inversion method amplifies the noise at high spatial frequencies. Many methods have been developed to solve Equation 1 iteratively, including least squares, maximum likelihood and wavelet-based methods. These algorithms typically require high-precision knowledge of the PSF, which we do not have for the BLAST05 maps. The effective PSFs vary significantly across the maps due to asymmetries in the beam-pattern (which itself is well-measured). Over time the orientation of this pattern on the sky changes, such that the effective shape of a point source depends on the amount of time spent observing at different parallactic angles, and instrumental noise variations. Iterative methods for deconvolution were attempted, but the variable PSFs proved to be too problematic. We concluded that strong artifacts due to convolution are inevitable and we decided to use the direct inversion method, even though it is probably non-optimal.

Equation 3 can be rewritten in real space as $\tilde{O} = I * K$, where K, the deconvolution kernel, is the inverse transform of $\hat{P}^{-1}$. In order to suppress the amplification of noise at high frequencies we effectively re-convolve the map by a Gaussian, G, with width approximately equal to the designed diffraction limit of the telescope. This can be combined with the deconvolution formulation by writing $\hat{K} = \hat{G}/\hat{P}$. Here $\hat{K}$ is also smoothed at large spatial frequencies to further suppress noise spikes as $\hat{P}$ goes to zero. Additionally, spikes in $\hat{K}$ due to zero-crossings in $\hat{P}$ are clipped.

The PSFs are estimated by two methods. In the first case, a synthetic PSF is constructed based on measurements of point sources throughout the flight. The synthetic PSF attempts to account for the range of parallactic angles over which the field

was observed by averaging together appropriately-weighted beam rotations. The second method uses a point source directly from the map. An isolated source from the north-west corner of the map is used (V05 in Figure 3), this having relatively low surrounding diffuse emission. A low-order polynomial is fit to the background and subtracted from the source to remove the diffuse emission. The deconvolutions are performed using both types of PSF. The synthetic PSFs provide the best results at 350 and $500\,\mu$m, while the isolated source is better for the $250\,\mu$m map, based on the amplitude of the ripples seen in the resulting deconvolved maps.

In order to reduce edge effects caused by the Fourier transforms, both the maps, I, and the PSFs, P, are apodized and zero-padded prior to deconvolution. The map is apodized over a scale of $5'$ along a rectangle bordering the map and the PSF is apodized over $2'$ along a circle of radius $4'$.

Finally, the variance map produced by SANEPIC is propagated through the deconvolution filter, providing a noise map for use in source-finding and fitting. The noise at each wavelength both before and after deconvolution are given in Table 1 under "Raw maps" and "Deconvolved maps" respectively.

2.5. Compact Source Identification

We search for individual compact sources in the deconvolved maps using source-finding analysis based on the use of a "compensated PSF", also called the Mexican Hat Wavelet (MHW) technique (see e.g., Barnard et al. 2004), which identifies objects in confused images by subtracting a local background. We apply the MHW with a characteristic width equal to the nominal resolution (the width of G in the deconvolution), to the BLAST deconvolved maps. The peaks of all ~ 6-σ clumps in each waveband are identified as potential sources. Due to the excess noise produced by the deconvolution process, many false detections are found near bright sources. No robust method to automatically reject these false peaks was found, since the ripples are not uniform across the image. We visually reject any peak that appears to be associated purely with the noise ripples. In addition, 11 of the recovered sources that lie slightly further away from the brightest objects remain clearly affected by these residual ripples. Since the ripples are different in each band the
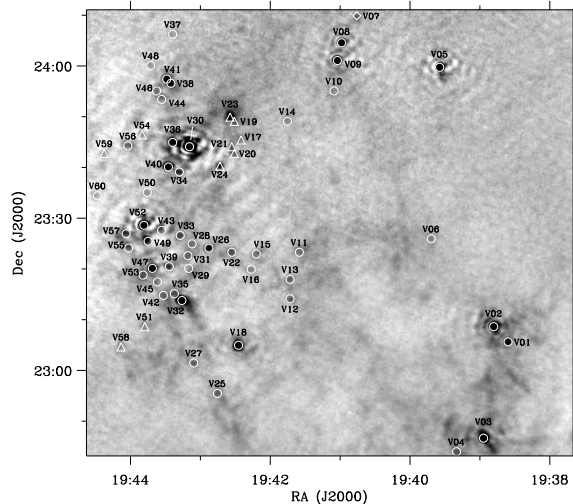
Fig. 3.— The grayscale image is a resolution enhanced BLAST $350\,\mu$m map, with the locations of compact sources (Table 2) indicated: 49 objects associated with the clouds surrounding NGC 6823 at ~ 2.3 kpc (circles); 10 objects in the Perseus Arm at ~ 8.5 kpc (triangles); and a single outer-galaxy object at ~ 14 kpc (diamond) — see §5 for a discussion of distance estimates. The resolution enhancement was accomplished with direct Fourier deconvolution of the PSF (see §2.4). Residual ringing is an artifact of uncertainties in the beam shape which varies slightly across the map.

8

net effect is to contaminate the observed BLAST colors. In total, $\sim 50\%$ of the rejected sources have formal statistical significances below 9-σ, although there is a tail of rejected sources extending to ~ 25-σ that have relatively higher systematic errors since they lie on the largest ripples next to the brightest submillimeter objects. The positions of BLAST sources derived from the deconvolved maps are shown in Figure 3.

The list of robust detections in each waveband are combined and a circular region around each peak in the three maps is then simultaneously fit with a single Gaussian. In addition nearby sources are fit using multiple Gaussians. In each region, a fourth order polynomial baseline is fit to the surrounding regions and subtracted. The amplitudes in each waveband, position, and width are all free parameters in the fit. The fit is calculated using a non-linear least-squares minimization routine. Constraints on source position and width are included to reduce the possibility of divergence in the fitting procedure. Leaving the source width as a free parameter in the fit biases the resulting flux densities high, but is necessary since the beam varies significantly across the field. This bias is investigated in the next section. Given the S/N of these sources, however, even after deconvolution, the flux density uncertainty is dominated by the calibration error. The catalog of source positions and BLAST flux densities are given in Table 2.

2.6. Monte Carlo Simulations

In order to estimate the effectiveness of our compact source extraction process, a series of Monte Carlo simulations are performed. Flux densities, biases, completeness estimates, and positional error distributions are investigated by inserting a point source, convolved with the estimate of the beam, into the actual BLAST maps produced with SANEPIC. The deconvolution and source extraction processes are applied and the extracted flux densities compared with the inputs. The source extraction routine is modified slightly from that described in §2.5 in order to avoid manually rejecting unreliable sources in residual ripples around bright sources — a simple automatic routine was implemented that is able to reproduce the manual rejection procedure for the original source list to an accuracy of $\sim 10\%$.

In order to extract the flux density bias and errors, 500 iterations are performed at each of several input flux densities spanning the range of source brightnesses found in the map. At each iteration, a $250\,\mu$m flux density is chosen and the 350 and $500\,\mu$m flux densities are assigned based on the median source colors found in the field. A simulated source is considered detected if an additional peak is found compared to the number of sources originally found in the map. In some cases, the simulated source will by chance land on top of a real source at the same position. In such cases, the detection of the simulated source is only counted if the flux density exceeds that of the real source that it obscures. The resulting output flux density distributions are roughly Gaussian with a positive tail. The Bayesian 68% confidence limits are found and the distributions are fit by the Gaussian that passes through these points. We find that the measured flux density is biased high by a factor of 1–1.2, independent of input flux density (Figure 4). Based on these results, we can describe the spread in flux density with a 2-component model: the first is independent of flux density, reflecting noise in the map, and the other is linear in flux density, due to uncertainty in the fitting process. Positional errors are calculated using the same simulations. These errors are described by circular Gaussians with σ ranging from $\sim 7''$ at the bright end to $\sim 70''$ at the faint end. Completeness is estimated using the same set of simulations, except that the flux density fits are not performed. At each of the input flux densities, 1000 simulations are performed and the number of times that the input is detected is counted. The results are shown in Figure 5.

In total, 60 compact sources are detected in the Vulpecula maps. Flux densities and their uncertainties are given in Table 2. Note that the tabulated values include a color correction based on SED fits; see §4.3 for a description of this procedure. Figure 3 indicates the positions of the detected sources.

3. INFRA-RED PHOTOMETRY

The BLAST data alone cannot accurately constrain the SED corresponding to thermal emission in many of the sources from this survey. At temperatures $T \gtrsim 25\,$K (and $\beta = 1.5$) all of the BLAST filters sample the Rayleigh-Jeans tail. To
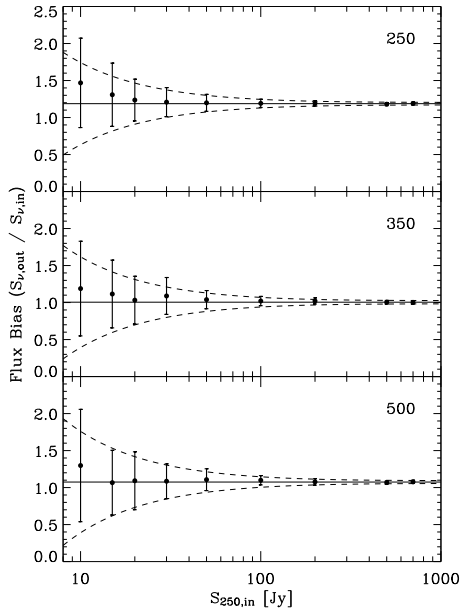
Fig. 4.— The flux density bias, determined from 500 Monte Carlo simulations, is shown for each waveband. The bias is modeled as a constant function of input source flux density and the errors are modeled with two components (described in §2.6).
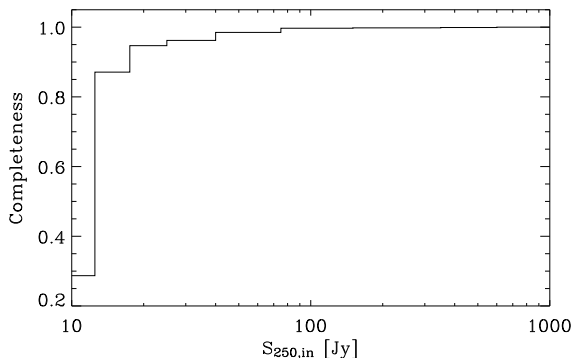

Fig. 5.— The completeness as a function of $250\,\mu$m flux density determined from 1000 Monte Carlo simulations (described in §2.6).

measure the luminosity and dust mass, additional photometry at slightly shorter wavelengths ($\sim$50–$100\,\mu$m) is required to identify the emission peak. FIR measurements and upper limits are estimated for all of the sources using *IRAS* 60 and $100\,\mu$m photometry and the new MIPS $70\,\mu$m map from MIPSGAL (Carey et al. 2005). Although most of the luminosity is produced at submillimeter and FIR wavelengths, a non-negligible portion is also observed in the mid-infrared (MIR) ($\lambda \sim$10–$50\,\mu$m). This radiation is emitted from hotter dust that lies close to the heat source. Protostars produce significant amounts of radiation in this band, since the material in the vicinity of the object is optically thick. This material is irradiated with UV light which is then re-emitted at longer wavelengths. To probe the MIR SEDs of BLAST sources we used *IRAS* 12 and $25\,\mu$m measurements and the *MSX* [1] catalog at 8, 12, 14, and $21\,\mu$m.

3.1. *IRAS* 12, 25, 60, and $100\,\mu$m Flux Densities

A significant fraction of the BLAST sources have clear counterparts in the *IRAS* Point Source Catalog version 2.0 (PSC, Helou & Walker 1988). We add the BLAST positional uncertainties in quadrature with the semi-major axes of the PSC error ellipse to determine search radii for each source. The BLAST uncertainties are taken from the simulations described in §2.6, but we conservatively set the error at the bright end to $30''$. Identifications from the *IRAS* PSC were found for 23 of the 60 BLAST sources, as summarized in Table 3.

For sources that lack PSC counterparts or measurements in any of the *IRAS* bands, we produce measurements or upper limits directly from *IRAS* maps. We use the *IRAS* Galaxy Atlas (IGA, Cao et al. 1997, at 60 and $100\,\mu$m) and the Mid-Infrared Galaxy Atlas (MIGA, Kerton & Martin 2000, at 12 and $25\,\mu$m). These maps are produced using the resolution-enhancing algorithm HIRES (Aumann et al. 1990). The PSFs vary across these maps, showing strong elongation along the scan direction. However, these HIRES maps resolve sources that are also detected with BLAST (see Figure 6) yet appear confused in *IRAS* maps that have not undergone resolution enhancement (e.g.,

---

[1] http://www.ipac.caltech.edu/ipac/msx/msx.html

the IRIS maps of Miville-Deschênes & Lagache 2005).

We use aperture photometry to measure flux densities in the IGA and MIGA maps. A circular aperture radius of $2'.4$ is used at $100\,\mu$m. For the remaining bands an elliptical aperture aligned with the scan direction is used, with semi-axes $1'.8 \times 1'.2$. These apertures are centred over the BLAST coordinates and the maps are integrated. Baseline pixel values are estimated as the median in an annulus between the outer-edge of the photometry aperture and a second circle (or ellipse) that is larger by a factor of 1.3. This size was chosen through trial-and-error as a compromise between smaller sizes which encompass fewer pixels (baseline estimates with larger statistical errors), and larger sizes which suffer greater contamination from large-scale extended structure or adjacent sources (baseline estimates with larger systematic errors). Since many of the sources remain confused, the flux density and baseline measurements are both checked visually. In cases where a small amount of emission is detected in the baseline annulus, the confused fraction is excised in the estimates. Furthermore, if additional sources are seen near the edge of the measurement aperture, or if it appears to lie on a bright gradient of background emission, the measurement is flagged as an upper-limit. Finally, if no source is visible in the aperture, it is flagged as a non-detection. The uncertainty in all of the measurements is estimated as the rms in the non-detections. The results of this photometry procedure are summarized in Table 4.

To verify our technique, we compare these aperture measurements with flux densities from the $IRAS$ PSC and find no significant bias, with scatters of 12% at $60\,\mu$m and 25% at $100\,\mu$m.

3.2. MIPS 70 μm Flux Densities

After examining the $IRAS$ PSC, and measuring flux densities in the IGA maps, 32 of the 60 BLAST sources lacked a clear detection at either 60 or $100\,\mu$m. To constrain the FIR SEDs in these cases, we use mosaics of the $70\,\mu$m MIPS-GAL (Carey et al. 2005) images downloaded from the $Spitzer$ public web site using the $Spitzer$ Pride software.[2] The $8\,\mu$m IRAC image (Figure 17) is

also produced using this software.

Similar to the flux densities obtained from $IRAS$ maps in §3.1, aperture photometry with baseline correction is used for the $70\,\mu$m map. The radius of the measurement aperture is $1'$ and the baseline aperture is an annulus with inner and outer radii of $1'$ and $1'.3$. It was noticed that these measurements yield flux densities systematically lower than the $60\,\mu$m observations, despite the fact that the SED for every source should be brighter at $70\,\mu$m, since these wavelengths fall on the Wien tail of the thermal emission in all cases. This problem arises because saturation and non-linearities affect MIPS $70\,\mu$m sources with flux densities $\gtrsim 20\,$Jy (A. Noriega-Crespo, private communication). Fortunately only the fainter BLAST sources require $70\,\mu$m photometry to constrain their FIR SEDs, and adopting a 20 Jy cut in the catalog of $70\,\mu$m measurements yields useful data for 10 BLAST sources with no $IRAS$ detections. The uncertainty in this photometry was estimated as 3 Jy from the rms of observations that were visually flagged as non-detections. A comparison between MIPS, $IRAS$, and BLAST is shown in Figure 6, and the MIPS photometry is summarized in Table 4.

3.3. 500–8 μm Map Comparison

Figure 6 shows an expanded view of a $0°.3 \times 0°.3$ region of the maps described in the previous sections, encompassing the BLAST sources V11, V12, V13, V15, and V16. It is clear that the relative brightnesses of sources vary greatly over the range 500–$8\,\mu$m, due to their different intrinsic SEDs. None of the BLAST sources in this region of the map have counterparts in the $IRAS$ PSC. Source confusion is also an issue; for example, although V12 is not in the $IRAS$ PSC, a counterpart is seen in the higher resolution IGA $60\,\mu$m and the MIPS $70\,\mu$m images (and MIGA as well). V16 has a faint counterpart at $70\,\mu$m. In the same images, $IRAS$ PSC sources not seen by BLAST appear: 19395+2313 between V11 and V13, 19397+2309 to the NE of V12, and 19399+2312 W of V16; the source SW of V15 is not in the $IRAS$ PSC. Based on the brightness and color of 19397+2309 at 60 and $100\,\mu$m (23 and 80 Jy respectively), we would expect to have detected this source with BLAST. Comparison of the $250\,\mu$m image with the $70\,\mu$m image (where the source is resolved into
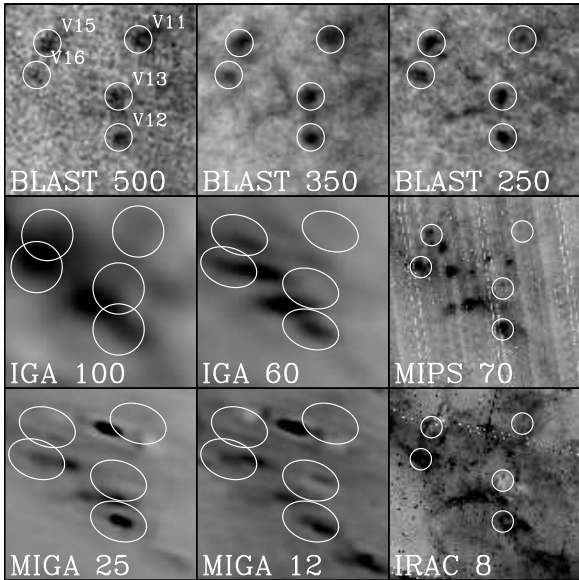
Fig. 6.— Comparison between BLAST05 deconvolved maps, *IRAS* maps produced with HIRES, and the *Spitzer* MIPS (70 μm) and IRAC (8 μm) maps. Each thumbnail has a size of $0°.3 \times 0°.3$. Circles on the BLAST maps and IRAC map indicate source positions with arbitrary diameters $2'.5$ and $2'$ respectively. The circles and ellipses indicated on the *IRAS* and MIPS maps are the apertures that were used for photometry. The SED of the coldest object, V11, is shown in Figure 8.

two), suggests a detection by BLAST, but it did not meet our compactness criteria to be tabulated as a point source. At even shorter wavelengths, additional sources and nebulosities appear, for example 19397+2315 E of V11.

3.4. *MSX* 8, 12, 14, and 21 μm Flux Densities

MSX flux densities for the BLAST sources are obtained from a cross-correlation with the *MSX* Point Source Catalog version 2.3 (Egan et al. 2003). As with the *IRAS* PSC (§3.1), *MSX* counterparts are identified within a search radius of the BLAST positions that varies as a function of the source brightness. The positional uncertainties in the *MSX* catalog are negligible by comparison (rms ~ 4–$5''$). We find potential *MSX* counterparts for 40 objects in the BLAST catalog. Inspection of the *MSX* maps shows that some of these sources are found in regions with diffuse emission, and, given the angular resolution of the BLAST catalog, we cannot presently determine whether all of the proposed *MSX* associations are BLAST objects, or other protostars in the same star forming region at an older evolutionary stage. In cases where a single *MSX* counterpart is identified we assume that it is in fact the same source. In cases with multiple proposed *MSX* counterparts, however, the sum of the flux densities is taken as an upper limit. Presently no attempt has been made to use the shape of the *MSX* SEDs to justify their associations with the BLAST objects. All candidates are given in Table 5.

4. SUBMILLIMETER–MIR SEDS

With submillimeter–MIR photometry, we fit the temperature and bolometric flux produced by the coldest dust, as well as the bolometric flux produced in the MIR. We note that all of our sources are likely composed of regions at different temperatures, typically a warmer core embedded in a colder and less dense medium. Our goal is to use a simple SED model as an interpolation function for the sparsely sampled photometry to estimate the total luminosity of each source, and to infer an approximate temperature for the dominant emission from cold dust.

We assume optically-thin emission from an

isothermal modified blackbody,

$$S_\nu = A \left(\frac{\nu}{\nu_0} \right)^\beta B_\nu(T), \qquad (4)$$

where A is the amplitude of the SED, $B_\nu(T)$ is the Planck function, β is the dust emissivity index, and the emissivity factor (brackets) is normalized at a fixed frequency ν_0. Note that the amplitude can be expressed in terms of a total clump mass, M_c, the dust mass absorption coefficient κ_0 (evaluated at ν_0), and the distance to the object, d,

$$A = \frac{M_c \kappa_0}{R d^2}. \qquad (5)$$

Since κ_0 refers to a dust mass, the gas-to-dust mass ratio, R, is required in the denominator to infer total masses. We adopt $\kappa_0 = 10 \, \text{cm}^2 \, \text{g}^{-1}$, evaluated at $\nu_0 = c/250 \, \mu\text{m}$, from Hildebrand (1983). A factor of 100 is assumed for R. We note that the combined mass uncertainty due to κ_0 and R is at least as large as a factor ~ 2 (e.g., Hildebrand 1983; Ossenkopf & Henning 1994; Kerton et al. 2001), depending on assumptions about the environment, age, chemical composition, and shape of the dust grains. Note that our adopted value, along with $\beta = 1.5$, is equivalent to the $1.2 \, \text{mm}$ opacity adopted by Motte et al. (2007).

Equation 4 is fit to all of the available photometry from 500–60 μm using χ^2 optimization (except for some cases where the FIR peak is very broad, in which case it is only fit from 500–100 μm). As in Truch et al. (2007) the band-averaged flux density of the model SED is calculated with knowledge of the BLAST filter passbands before comparing them with measurements. We also include the correlated calibration uncertainties with the statistical uncertainties estimated in §2.6. The data covariance matrix, C, is constructed by placing the estimated variance for each data point along the diagonal. For the BLAST data points, the diagonals are calculated as the quadrature sum of the statistical uncertainties with the calibration uncertainties listed in Table 1 in Truch et al. (2007). The off-diagonal cross-correlation terms are estimated directly from the Pearson correlation coefficients in the same table. β is not well constrained and is therefore fixed to $\beta = 1.5$ (consistent with Figure 9) so that only A and T are allowed to vary.

For the 11 cases where the BLAST colors are unreliable (§2.5; marked in Table 2), a temperature of $20 \, \text{K}$ has been adopted.

4.1. Including Upper Limits in χ^2

Many of the fainter sources have only BLAST detections. In order to make the best use of FIR upper-limits, "survival analysis" is used to include the upper-limits in the calculation of χ^2. Given a measurement that is deemed an upper limit, with flux density, s_l, and uncertainty, σ_l, the likelihood of the model flux density, $\tilde{s}$, is obtained from the integral of the appropriate tail of the likelihood of a detection,

$$p(\tilde{s}|s_l, \sigma_l) = \frac{1}{\sqrt{2\pi}} \int_{(\tilde{s}-s_l)/\sigma_l}^{\infty} e^{-z^2/2} dz, \qquad (6)$$

where we have assumed Gaussian noise. Equation 6 is the "survival function" for censored data (Isobe et al. 1986). The behavior of this function is easily seen with a few examples. If the model flux density is much smaller than the measured limit, then the likelihood goes to 1. If the model is equal to the measured limit, the likelihood is 0.5. The likelihood of models more than a few σ above the limit drops to ~ 0.

Noting that χ^2 is the negative log-likelihood function, and assuming the likelihood of the upper limits is independent of the detections, then

$$\chi^2 = (\tilde{s} - s_d) C^{-1} (\tilde{s} - s_d)^T - \ln p(\tilde{s}|s_l, \sigma_l). \qquad (7)$$

Here s_d are the measured detections associated with the data covariance matrix, C. Equation 7 gives the expression that we minimize in order to fit the region of the data consistent with the isothermal SED model ($\gtrsim 60 \, \mu$m).

4.2. SED Fits

Uncertainties for the model parameters A and T, and non-linearly dependent quantities such as the FIR integrated flux, M_c, and their distance-independent ratio L_{FIR}/M_c, are obtained from Monte Carlo simulations. Mock data sets are generated from realizations of Gaussian noise, including both correlated and uncorrelated errors, as described by the covariance matrix. The χ^2 minimization process is repeated for each data set, and the resulting parameters and dependent quantities

placed in histograms. Means and 68% Bayesian confidence intervals measured from the relevant histograms are given in Table 6. Note that errors in T have opposite effects on L_{FIR} and M_{c}, which exaggerates the uncertainty in $L_{\mathrm{FIR}}/M_{\mathrm{c}}$.

Figure 7 shows an example SED for V30, the brightest BLAST object in the sample. The solid gray lines indicate the 68% confidence envelope of modified blackbodies that fit the BLAST and *IRAS* 100 μm data. The black line consists of the best-fit modified blackbody at wavelengths $> 100\,\mu$m, and a series of piecewise-continuous power-laws through the *IRAS* and *MSX* data points at wavelengths $\leq 100\,\mu$m. The best fit temperature to the submillimeter data is 26 K, considerably smaller than 46 K estimated from MIR and mm data away from the peak (Sridharan et al. 2002). The luminosity fraction given in column 5 of Table 6 is the ratio (as a percentage) of the FIR integrated flux from the best-fit modified blackbody (solid gray lines) to the total bolometric flux, estimated from the integral of the black line across the wavelength range 2–5000 μm. Similarly, Figure 8 shows the SED of V11, the coldest object in the sample ($T = 12.3\,$K). As seen in this example, observations across the BLAST wavelength range clearly reveal a turnover in the FIR SED for the coldest objects. The lack of counterparts in the shorter-wavelength bands is emphasized in Figure 6.

The range of modified blackbody models from the Monte Carlo simulations are generally very tight (e.g. for V30 $\Delta T = 1.0\,$K, and for V11 $\Delta T = 1.6\,$K). The narrowness of this range is largely due to the prior constraint that the dust emissivity index is precisely $\beta = 1.5$. There is a strong degeneracy between the values of β and T; for example, at larger values of β the steepness of the Rayleigh-Jeans spectrum increases, requiring lower values of T to compensate for that steepness, by bringing the FIR peak to longer wavelengths and hence closer to the shape of the data reported in the BLAST bands. For the two examples discussed here, we re-fit the $\lambda \geq 100\,\mu$m region of the SED, letting A, T, and β vary independently in 100 Monte Carlo simulations. For V30 the resulting range of temperatures and dust emissivities are $T = 27.6 \pm 2.8\,$K, and $\beta = 1.4 \pm 0.3$ (compared with $T = 25.9 \pm 1.0\,$K when $\beta = 1.5$). For V11 the ranges are $T = 9.4 \pm 3.4$ and $\beta = 2.9 \pm 1.5$ (com-

pared with $T = 12.3 \pm 1.6$ when $\beta = 1.5$). Particular realizations from these Monte Carlo simulations have been selected to illustrate the approximate 1-σ range of T as dashed gray lines in Figures 7 and 8. Many of the BLAST sources have poorly constrained values of T and β as in the example of V11. We have therefore chosen to fix $\beta = 1.5$ for the remainder of the analysis in this paper, which reduces inferred errors in T by factors of $\sim$ 2–3. It also emphasizes the range of SEDs uncovered by BLAST, since under this constraint T uniquely determines the wavelength of the FIR peak.

In addition to the effect of the prior on β, the treatment of correlated uncertainties between the BLAST measurements lead to inferred temperature ranges that are perhaps smaller than what one might expect given the sizes of the error bars in Figures 7 and 8. For example, V30 has photometric errors that are only $\sim$ 2% in all three bands (Table 2). However, the error bars shown in these figures include approximately $\sim$ 10% calibration uncertainties that are nearly 100% correlated across the three bands. This type of uncertainty only affects the absolute *scale* of the SED, A, but not the *shape* which is encoded in T and β (for which only the independent 2% photometric errors are relevant). For this reason the temperature uncertainty in V30 (under the model assumptions) is only $\Delta T = 1.0\,$K, demonstrating the superior ability of BLAST to constrain the shape of the FIR SED of cold sources when systematic uncertainties are accounted for appropriately.

4.3. Color-corrected BLAST Flux Densities

BLAST filters have broad spectral widths that are $\sim$ 30% of the central frequency (Pascale et al. 2007). Since colors sampled by the filters are a strong function of temperature for cooler objects ($T \lesssim 25\,$K), a color correction is required to enable direct comparison with SEDs. Once the SED (Equation 4) has been fit to data by minimizing χ^2 (Equation 7), we have the choice of either calculating different effective wavelengths for each measurement, or correcting each flux density at fixed wavelengths. We choose the latter, and correct the flux densities to precisely 250, 350, and 500 μm (this procedure is described in Truch et al. 2007). These corrected flux densities are given in Table 2,
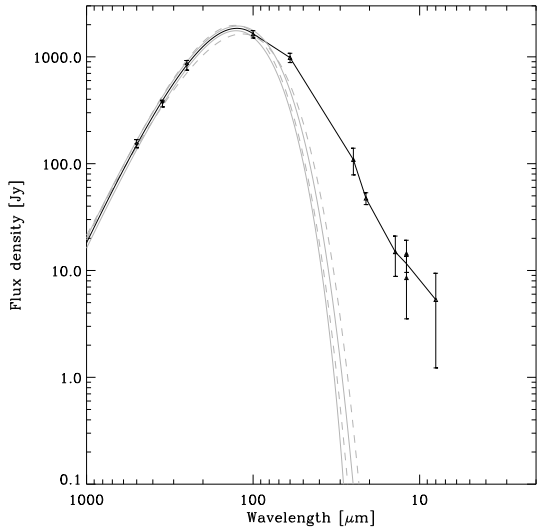
Fig. 7.— Example SED for V30, the brightest BLAST object ($T = 25.9$ K). BLAST error bars include correlated calibration uncertainties ($\sim$10%). Gray lines show the 68% confidence envelope of modified blackbody models from Monte Carlo simulations in which the dust emissivity index is fixed at $\beta = 1.5$. Dashed gray lines are particular realizations from a second Monte Carlo simulation in which β is also left as a free parameter, here indicating the 1-σ envelope of T (§4.2). The black line shows the best-fit modified blackbody connected continuously at $100\,\mu$m to a series of piecewise-continuous power-laws between the shorter-wavelength data.
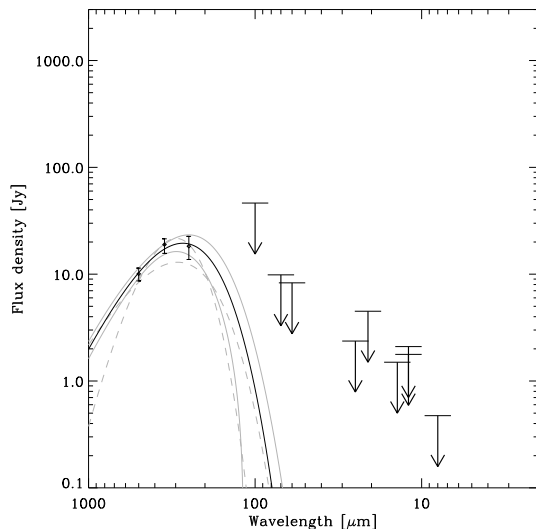
Fig. 8.— Example SED for V11, the coldest BLAST source ($T = 12.3$ K). Symbols have the same meaning as in Figure 7. The FIR spectrum clearly turns over in the BLAST bands, and there are no detections at the *IRAS*, MIPS or *MSX* wavelengths (see Figure 6). The bolometric flux for this source can only be crudely estimated from the integral of the modified blackbody.

and a color-color plot for all 60 sources is shown in Figure 9. This plot illustrates the variation in temperatures probed by the BLAST wavelengths, and confirms that the choice of $\beta = 1.5$ for the SED fits is close to the center of the distribution. We have also tested the color-correction method using $\beta = 1$ and $\beta = 2$ and find that the effect on the measured flux densities is small compared with the photometric uncertainties.

4.4. Distance-independent Clump Properties

The range of temperatures inferred from the SED fits to BLAST data with reliable colors is shown in Figure 10. The survey has convincingly detected sources with a range of FIR peak wavelengths, since the temperature span, $10\,\mathrm{K} \lesssim T \lesssim 40\,\mathrm{K}$, is much larger than the individual uncertainties that are typically ~ 1–$2\,\mathrm{K}$ (Table 6). It should be noted that these latter uncertainties characterize the range of plausible temperatures *under the assumption of the simple SED model* (Equation 4). There is also a systematic dependence on β; for example, increasing β from 1.5 to 2.0 shifts most temperatures lower by about $5\,\mathrm{K}$, and derived masses higher by a factor of ~ 2. Further details on correlations are given in §4.2.

As described above, the luminosity-to-mass ratio can also be calculated from the SED fits without any knowledge of the distance. For the simple SED model adopted, $L_{\mathrm{FIR}}/M_{\mathrm{c}} \propto T^{4+\beta}$ and so we find a broad range in $L_{\mathrm{FIR}}/M_{\mathrm{c}} \sim 0.2$–$130\,\mathrm{L}_\odot\,\mathrm{M}_\odot^{-1}$ for the objects with T in the range $12 - 40\,\mathrm{K}$ (Figure 10).

5. DISTANCES

To deduce luminosities and masses one must have an estimate of the distance to each source. There is, however, little information in the literature regarding distances to known objects in this field. Cross-correlation with the *IRAS* PSC identifies 23 of the 60 BLAST sources with known objects (Table 3). While some of these sources have been studied extensively (Beuther et al. 2002; Beltrán et al. 2006), few have unambiguous distance information. Important clues are provided by the morphology and velocity of the interstellar material and their inter-relationship. We have carried out a multi-wavelength assessment com-
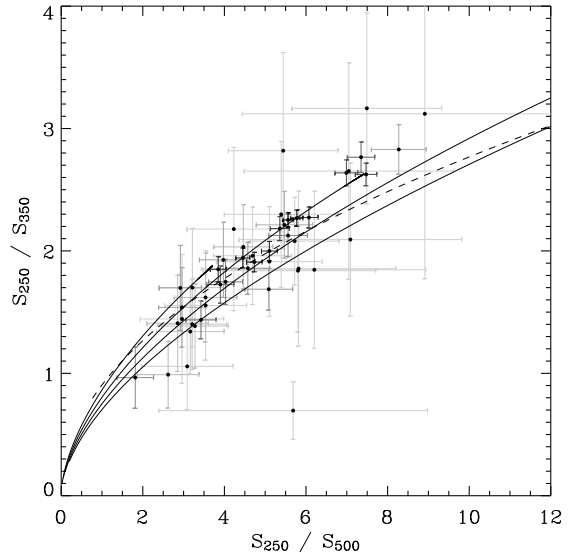
Fig. 9.— Color-color plot for the compact sources detected by BLAST05. We have omitted several sources with unreliable colors, identified in Table 2, and two sources with highly unconstrained colors due to faint flux densities. Modified blackbody models with constant β, equal to 0, 1, 2, and 3, increasing towards the bottom, and temperatures ranging from 5 to $200\,\mathrm{K}$ are overplotted as solid lines. The dashed line represents the same model with a constant temperature of $20\,\mathrm{K}$ and with β ranging from -1 to 3. The 1-σ statistical error bars are shaded so that the more significant detections are darker. The flux densities plotted have been band-corrected as discussed in §4.3.
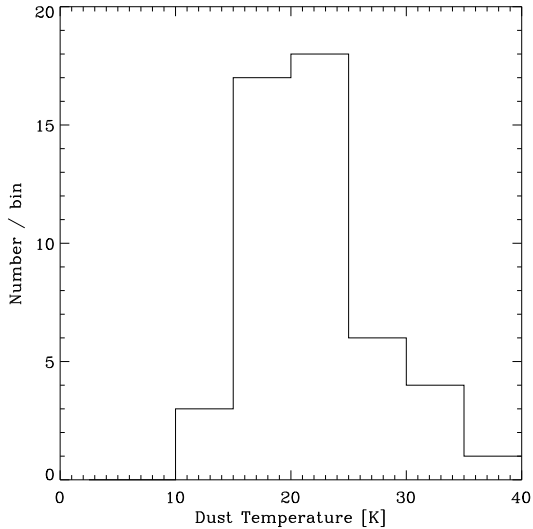
Fig. 10.— Histogram of inferred dust temperatures, assuming a dust emissivity index $\beta = 1.5$, and excluding 11 objects for which the BLAST colors are considered unreliable. The entire distribution shifts downward by $\sim 5\,$K if instead $\beta = 2.0$ is adopted (uncertainties are discussed in §4.2).

paring the BLAST images and point sources with *IRAS* (Cao et al. 1997; Kerton & Martin 2000); *MSX*; IRAC (§3.2); the STScI Digitized Sky Survey[3] (DSS); 21 cm radio continuum imaging from the VLA Galactic Plane Survey (VGPS, Stil et al. 2006); and spectral line imaging in ^{13}CO (1→0) (FCRAO: Brunt & Heyer 2007) and H I (VGPS).

We argue below that 49 of the 60 BLAST sources in this field are associated with the molecular cloud complex within which the open cluster NGC 6823 has already formed (Figure 2). We are then able to adopt the photometric distance measured for the stars. We use 2.3 kpc (Massey et al. 1995), though we note that distances in the range 1.5 to 3.2 kpc have been reported (Hoyle et al. 2003; Guetter 1992; Peña et al. 2003). In a program measuring parallaxes using methanol masers (Menten 2007) a distance of $2.20 \pm 0.01\,$kpc is found for the masers associated with V30 (IRAS 19410+2336; see Szymczak et al. 2000), about 0°.5 from the cluster center. NGC 6823 is placed in a Galactic context in Figures 11 and 12. In nei-

ther position nor velocity (see below and Lockman 1989, Figure 2) is it part of the main Sagittarius arm. In addition ten of the sources appear to be in the more distant Perseus arm ($\sim 8.5\,$kpc), and a single object (V07) is thought to lie beyond that in the outer galaxy ($\sim 14\,$kpc). The sources that are not associated with the NGC 6823 molecular complex are indicated thus in Table 2.

The *IRAS* images (see Figure 1) show that the bright sources and diffuse emission represent a distinctive enhancement of size $\sim 2°$, which as we discuss below is also the scale of the coherent molecular complex. However, within the complex there is sub-structure, both in space and velocity. The angular diameter of the NGC 6823 cluster is $\sim 0°.5$ (Kharchenko et al. 2005), and this is a part of the overall complex. The diffuse radio and optical emission from the H II region Sh2-86 (LBN 135), the portion of the complex that is being ionized, is also of this size. Within this region there are ionization fronts, clearly associated with the ionizing stars in NGC 6823, sculpting the parent molecular material. A particularly striking example that can be seen in the red DSS image is a silhouetted "pillar" pointing at the stars, with an ionization front at its end and V39 immediately behind it. V43 and V49 are other similar examples.

At 2.3 kpc, $\sim 2°$ corresponds to a physical size of 80 pc, so that all of the parts of the complex are at essentially the same distance to within a few percent (there could be a systematic error in the average distance, as noted), with variations indicated by slightly different velocities or a silhouette indicating relative position along the line of sight.

To introduce the velocity scale, the radio recombination line velocity of Sh2-86 measured by Lockman (1989) in a 9′ beam is $29.4 \pm 2.1\,$km s^{-1} with FWHM $24.2 \pm 2.9\,$km s^{-1}. This velocity width, greater than a typical thermal width, and typical of widths found in that survey, could reflect accelerated gas motions in the ionized material and/or be intrinsic to the original neutral components comprising this star forming complex. It is certainly unrelated to differential Galactic rotation. For a distance of 2 kpc, the gradient in the rotation curve (Figure 12) is $\sim 125\,$pc km^{-1} s, and so the velocity spread would in that interpretation imply a cloud of extreme elongation along the line of sight. Note that this velocity and distance combination does not fall on the mean rotation curve.

---

[3]http://archive.stsci.edu/dss/
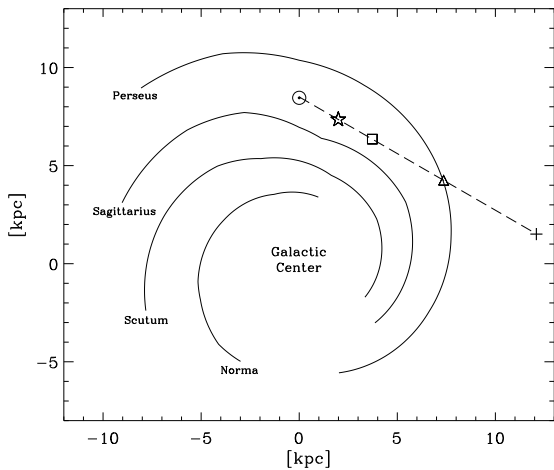
Fig. 11.— Galactic spiral arm model of Taylor & Cordes (1993). The dashed line indicates the line of sight towards 60° longitude. The star indicates the location of the open cluster NGC 6823 at the adopted distance of 2.3 kpc (Massey et al. 1995). We associate 49 of the 60 BLAST sources with the molecular complex within which NGC 6823 has already formed. Another 10 "Perseus arm sources" are approximately 8.5 kpc distant (triangle) and one object (V07) appears to be in the outer Galaxy (plus). The square indicates the tangent point.

There are substantial systematic motions in this direction, including considerable emission of both ^{13}CO and H I beyond the nominal tangent-point velocity ($\sim 34\,\mathrm{km\,s^{-1}}$) and so kinematic distances from the rotation curve in this range are unreliable.

5.1. Velocities

Using the accurate BLAST source positions, we have examined ^{13}CO (1→0) spectra of Vulpecula, having 46″ spatial and $1\,\mathrm{km\,s^{-1}}$ velocity resolution (binned from a native resolution of $0.13\,\mathrm{km\,s^{-1}}$), respectively. Generally a single compact spatial/spectral coincident feature is identified (see the example of source V12 in Figure 13). We therefore fit Gaussian profiles to the velocity component at the position of each source. The lines at BLAST positions have a typical FWHM of $2.5\,\mathrm{km\,s^{-1}}$. Ten of the BLAST/*IRAS* counterparts have previously-measured velocities in other spectral lines, specifically CS (Beuther et al. 2002; Bronfman et al. 1996) and NH$_3$ (Molinari et al. 1996; Sridharan et al. 2002; Zinchenko et al. 1997). Our measured velocities for these objects are on average within $1\,\mathrm{km\,s^{-1}}$ of the published velocities, the maximum deviation being $2\,\mathrm{km\,s^{-1}}$. The velocities are listed in Table 2 and are presented in Figure 14. The broad peak from 21 to $36\,\mathrm{km\,s^{-1}}$ is similar to that seen in the average spectrum of this region, which also includes more diffuse gas. The ^{13}CO velocity of V06, at $43\,\mathrm{km\,s^{-1}}$, still falls well within this range.

Several BLAST sources are in molecular clumps that clearly affect the radio emission from the extended H II region Sh2-86 seen in Figure 15. For example, V32 is a clear local minimum surrounded by an ionization front. The pair V22 and V26 are also at a minimum. Other objects apparently shaping or influencing the steepness of the radio contours are V47, V49, and V52. All of these sources have CO clump velocities in the range 26–$31\,\mathrm{km\,s^{-1}}$, like the radio recombination line velocity.

V23 (with V19 close by) is coincident with a bright compact H II region and has the weakest CO signature of all the BLAST sources. Additional velocity information for V23 was obtained using H I absorption against the radio continuum source using VGPS data. Velocity components are identified at −5, 7.5, 21 (very strong), 27, and
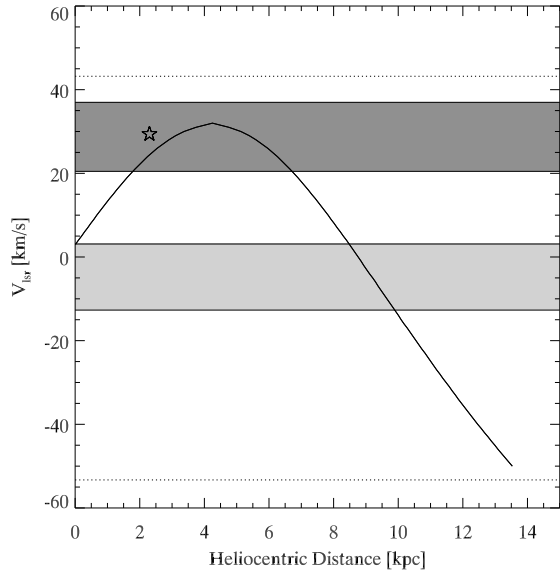
Fig. 12.— The solid curve shows the expected kinematic distance-velocity relationship derived from the Galactic rotation curve of Brand & Blitz (1993) projected along $\ell = 60°$. At the adopted distance of 2.3 kpc for NGC 6823 we show the average radio recombination line velocity of Sh2-86 as a star. The dark shaded region indicates the spread of ^{13}CO velocities measured for the BLAST sources associated with the main cloud complex. The uppermost dotted line indicates the velocity of V06, which is higher than the main spread but still consistent with systematic motions around the mean. The light shaded region indicates the "Perseus arm sources" and the lowest line the source V07 in the outer Galaxy.
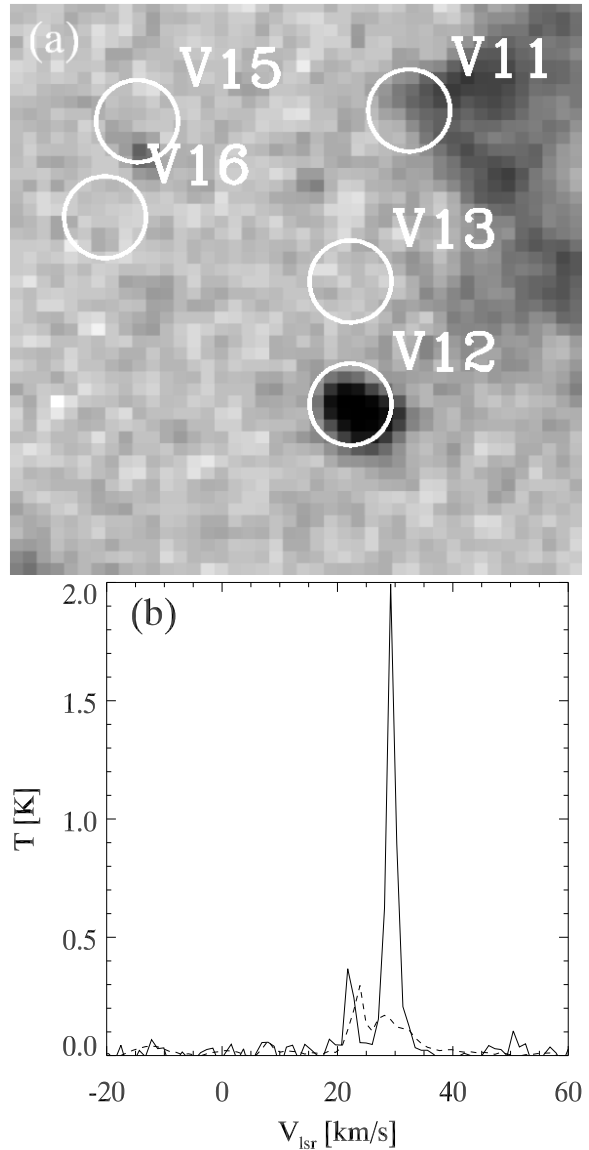
Fig. 13.— (a) Channel image of ^{13}CO at a velocity of 29 km s^{-1} for the region shown in Fig. 6. (b) Plot of ^{13}CO spectrum averaged over 9 pixels centered on V12 (solid line) and average over whole region in panel a (dashed). The bright clump is compact (has a high contrast) both spatially and in velocity, making it reasonable to identify it with the BLAST source (Table 2).

19
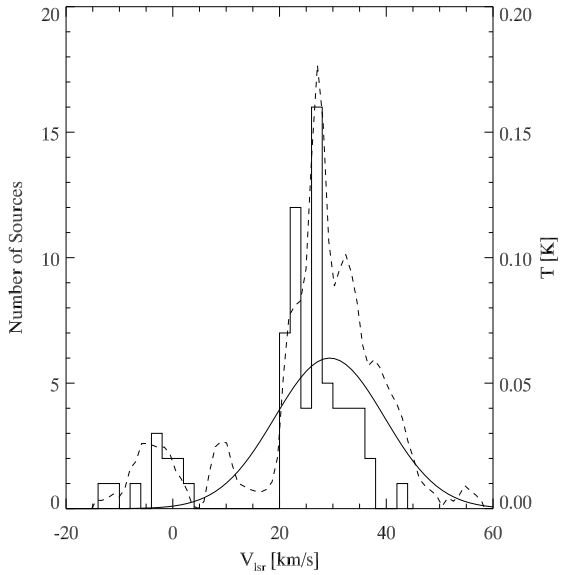
Fig. 14.— Histogram of the ^{13}CO radial velocities associated with BLAST sources. The majority of these velocities are very similar to the radio recombination line velocity of the H II region Sh2-86 measured by Lockman (1989), shown as the Gaussian (with arbitrary normalization). The dashed line indicates the average spectrum of the entire ^{13}CO map, including more diffuse gas. The peak at $10\,\mathrm{km\,s^{-1}}$ is the fairly structureless local gas, and that at $-5\,\mathrm{km\,s^{-1}}$ is the Perseus arm in which we identify 10 sources.
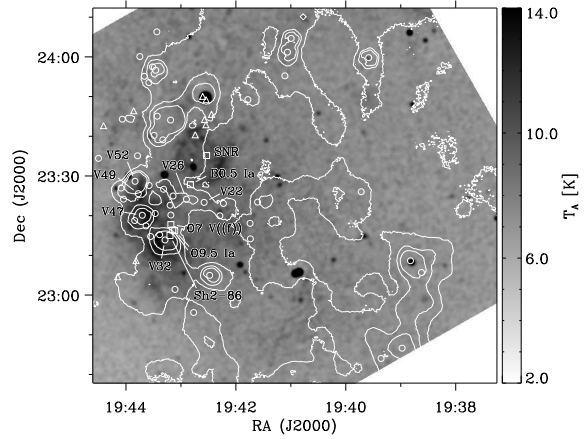
Fig. 15.— The grayscale shows the VGPS 21-cm radio continuum emission, which dominated by a structured H II region Sh2-86 and a shell supernova remnant (diameter $\sim 15'$, Taylor et al. 1992). Overplotted are the BLAST $350\,\mu$m contours, which reveal the interfaces between thermal dust emission (neutral material) and the ionized gas. Circles (sources associated with NGC 6823) and triangles (Perseus arm sources) identify the compact BLAST sources. The squares indicate the most massive stars in the open cluster NGC 6823. Labeled BLAST sources (V22, V26, V32, V47, V49 and V52) lie in molecular clumps that clearly affect the radio emission from Sh2-86.

$31\,\mathrm{km\,s^{-1}}$. The radio recombination line velocity in a $3'$ beam (Lockman 1989) is $-2.8 \pm 1.8\,\mathrm{km\,s^{-1}}$ with FWHM $15.2 \pm 2.6\,\mathrm{km\,s^{-1}}$(the unusually low line width suggests an electron temperature less than $5000\,\mathrm{K}$). The spatial position of V23 with respect to the main CO complex and other *IRAS* and BLAST sources suggest it is at the same distance, but the velocities at -5 and $-2.8\,\mathrm{km\,s^{-1}}$ indicate a much larger distance $\sim 9\,\mathrm{kpc}$ just beyond the solar circle in the Perseus arm. Nearby, V20 and V24 have similarly low velocities, appearing along a clumpy arc of $^{13}\mathrm{CO}$ emission at -3 to $+2\,\mathrm{km\,s^{-1}}$. V17 and V21, which have $^{13}\mathrm{CO}$ components near $\sim 0\,\mathrm{km\,s^{-1}}$ that are comparable in strength to weak components in the nominal NGC 6823 molecular cloud velocity range, are probably in this distant cloud too. We shall call these the "Perseus arm sources."

The only other BLAST source for which we can measure the H I absorption directly is V02. It has strong sharp absorption at 31 and $35\,\mathrm{km\,s^{-1}}$ and weaker components at $10\,\mathrm{km\,s^{-1}}$, and possibly -6 and $+43\,\mathrm{km\,s^{-1}}$as well. The $^{13}\mathrm{CO}$ velocity of this clump is $32\,\mathrm{km\,s^{-1}}$, but there is considerable gas near $\sim 40\,\mathrm{km\,s^{-1}}$ in the surrounding cloud on this side of the map.

There is a weak radio source that is coincident with V07 and a molecular clump at $-54\,\mathrm{km\,s^{-1}}$. This source is too faint in the radio for any possibility of measuring H I absorption. We use the rotation curve (Figure 12) to find a kinematic distance of $14\,\mathrm{kpc}$, making this an intrinsically luminous star forming region in the outer Galaxy.

On the low side of the velocity distribution, there are a few other sources with $^{13}\mathrm{CO}$ components near $\sim 0\,\mathrm{km\,s^{-1}}$ that are comparable in strength to weak components in the nominal NGC 6823 molecular cloud velocity range, namely V51, V54, V58, and V59. Using $\mathrm{C^{18}O}$ spectra (Brunt & Heyer 2007), which probe even denser gas, the low velocity component is chosen for V51 and V58 (these join the Perseus arm sources). V54 and V59 are seen in projection near the lower outskirts of the NGC 6823 cloud, as depicted in the zeroth-moment image (Figure 16). Since there is no compelling morphological evidence to relate them to the higher-velocity gas, we also consider them to be Perseus arm sources.

Finally, we note a puzzling result. Using the H I absorption technique to break the distance

ambiguity, and Arecibo observations (with a $4'$ beam) at the Sh2-86 position (Lockman 1989), Kuchar & Bania (1994) find absorption in the spectrum out to $50\,\mathrm{km\,s^{-1}}$and so adopt the far distance solution 6.3 kpc. Certainly, there is no question about the velocity of the H II region and hence the associated molecular cloud and BLAST sources. But as we have mentioned above, the ionization fronts seen on the DSS protruding into the molecular cloud are clearly caused by the bright OB stars in NCG 6823 identified by Massey et al. (1995), and these have a photometric distance much closer to the near solution. We have looked at the VGPS H I data (also with continuum, and $1'$ spatial resolution) across the face of the radio nebula. We find that there are large changes in the emission and absorption spectrum, with some absorption to 50 $\mathrm{km\,s^{-1}}$(in line wings) even at the fainter western edge, where the continuum emission blends into the (non-zero) background. This suggests that there is variable distant background continuum emission that is making it difficult to apply the technique on this extended source.

5.2. Morphology

A map of the $^{13}\mathrm{CO}$ emission integrated over the velocity interval 21–$36\,\mathrm{km\,s^{-1}}$ is shown in Figure 16. Figure 17 shows the IRAC $8\,\mu\mathrm{m}$ image for comparison. These both trace neutral material, but the latter, heavily influenced by PAH emission, requires illumination by sub-ionizing ultraviolet radiation (rather than simply tracing column density). Also, $8\,\mu\mathrm{m}$ is a short enough wavelength for there to be extinction by large column densities, producing the infra-red dark cloud (IRDC) phenomenon (Egan et al. 1998; Simon et al. 2006). A portion of the molecular cloud associated with V03 and V04 produces a local minimum in the diffuse $8\,\mu\mathrm{m}$ emission, suggesting it is in the foreground. On a smaller scale, V13 and V56 appear to exhibit similar behavior.

Overlaid on the figures are the BLAST $350\,\mu\mathrm{m}$ contours, which reveal excellent correspondence between this measure of the neutral column density and the other tracers. Also indicated are the BLAST point sources and the ionizing stars in NGC 6823 (Massey et al. 1995).

A particularly striking filament, which is a prominent dust lane in the red DSS image, is seen as a ridge in the BLAST, $^{13}\mathrm{CO}$, and IRAC maps
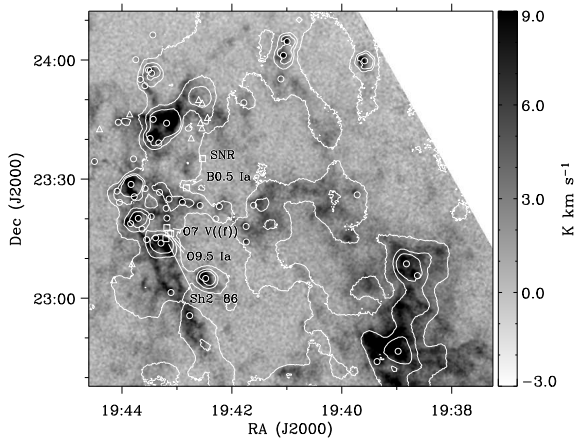
Fig. 16.— The grayscale shows the ^{13}CO emission integrated over 21 to $36\,\mathrm{km\,s^{-1}}$. Overplotted are the BLAST $350\,\mu$m contours which demonstrate a close correspondence between thermal dust emission and molecular gas in this velocity range. Circles (sources associated with NGC 6823) and triangles (Perseus arm sources) identify the compact BLAST sources. The squares indicate the most massive stars in the open cluster NGC 6823. Also indicated is the position of the supernova remnant, and the extended H II region Sh2-86.
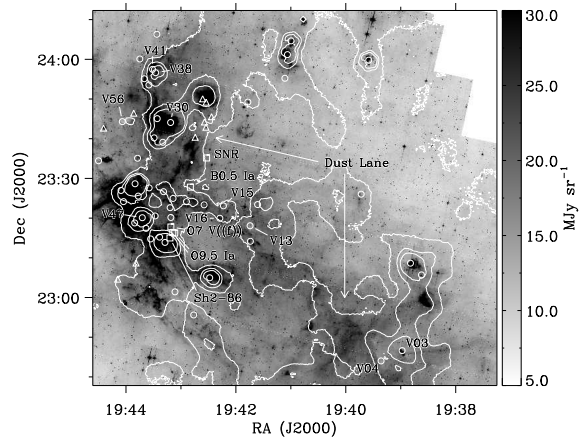
Fig. 17.— The grayscale shows IRAC $8\,\mu$m emission, with the same annotations as Figure 16. We note that the labeled BLAST sources (V03, V04, V13, and V56) occur at minima in the diffuse $8\,\mu$m emission, possibly indicating that the submillimeter objects are (associated with) infra-red dark clouds somewhat in the foreground. A prominent filament which appears as a dust lane in the red DSS image is also indicated (probably related to the BLAST sources V13, V15, V16, V38, and V41). Optical absorption is also associated with V47. These features are discussed in §5.2.

(indicated in Figure 17), running from V30 to the south west (parallel to the Galactic Plane) toward V03. BLAST sources V13, V15, V38, V41, and possibly V16 appear to be related to this optically-dark filament. Other optical absorption is associated with BLAST source regions, such as V47 projected on the H II region.

An interesting phenomenon seen in the H I data is self-absorption (HISA), caused by colder foreground material; it is most convincingly found using the criteria of narrow lines and fine-scale spatial structure (Gibson et al. 2000) but can also be more widespread. HISA appears at $24 \, \mathrm{km \, s^{-1}}$ in this filamentary structure. Near $33 \, \mathrm{km \, s^{-1}}$ there is striking filamentary HISA which extends into the V22–V26–V28 portion of the molecular complex, where the lack of H I emission no doubt also reflects a real deficit. At $36 \, \mathrm{km \, s^{-1}}$ there is more HISA which traces the diffuse submillimeter emission along the ridge ending at V06. This ridge is evident in $^{13}\mathrm{CO}$ at these velocities, but is not so clearly seen with IRAC.

Examination of the sequence of channel maps in the $^{13}\mathrm{CO}$ data cube, or the first moment (average velocity) map reveals a velocity gradient from the north-east to the south-west (higher to lower Galactic longitudes). Along the long filament the velocity changes quite systematically, indicating a large scale connectivity between the different portions of the molecular complex.

Also revealed in these data are large areas of low emission. To the west of the stellar cluster is a distinctive void, cleared of molecular gas and dust. As expected, because the gas has become molecular, there is a general deficit of H I across this entire region. This can be seen extending to adjacent longitudes in the longitude-velocity diagram of Stil et al. (2006). The deficit is exaggerated adjacent to the H II region (near $33 \, \mathrm{km \, s^{-1}}$ where the gas is molecular). This can appear more localized too, e.g., near V03 and in the V08–V09 cloud at the same velocity as the $^{13}\mathrm{CO}$.

Another void coincides with a supernova remnant found by Taylor et al. (1992) and is seen in finer detail in the VGPS radio continuum image (Figure 15). The void is seen in H I and in $^{13}\mathrm{CO}$ as well near $22 \, \mathrm{km \, s^{-1}}$. The remnant is not noticeably interacting with the surrounding dense material (e.g., no steepening of the $^{13}\mathrm{CO}$ contours or brightening or deformation of the radio shell), and

so perhaps the supernova occured in a pre-existing cavity, rather than creating it. The diameter of the remnant is only $0°.2$ ($8 \, \mathrm{pc}$) and so it could be at the average distance of this cloud complex (as the velocity suggests) but not yet have encountered one of its clumpy components.

6. DUST MASSES AND LUMINOSITIES

In §5 we determined distances for all of the objects: 49 are associated with the open cluster NGC 6823 at $\sim 2.3 \, \mathrm{kpc}$, 10 with the Perseus arm at $\sim 8.5 \, \mathrm{kpc}$, and 1 object is in the outer galaxy at $\sim 14 \, \mathrm{kpc}$ (summarized in Table 2). Here we use these distance estimates to convert the integrated fluxes from §4 into bolometric luminosities, L, and to derive the mass, M_c, for each source.

The clump mass M_c given in column 3 of Table 6 has been obtained from Equation 5. Note that although a mass absorption coefficient at $250 \, \mu\mathrm{m}$ appears in this expression, A is derived from the fit to the entire submillimeter and FIR data, rather than just the single color-corrected BLAST $250 \, \mu\mathrm{m}$ data point alone.

The masses of the clumps discovered range over ~ 15–$700 \, \mathrm{M_\odot}$ in NGC 6823, extending to somewhat higher masses in the Perseus arm. These sources are by definition compact in the submillimeter (and they are compact in CO as well), with characteristic sizes $D < 0.44 \, \mathrm{pc}$ at $2.3 \, \mathrm{kpc}$ (taking the de-convolved $250 \, \mu\mathrm{m}$ map beam size of $40''$ from Table 1 as a limit). If observed at higher resolution many of these "clumps" would probably qualify as "cores" in the terminology of Zinnecker & Yorke (2007). The column density for a typical $100 \, \mathrm{M_\odot}$ clump, assuming a uniform sphere limiting diameter D, is of order $10^{23}(0.44 \, \mathrm{pc}/D)^2 \, \mathrm{cm^{-2}}$ (visual extinction to the cloud center $A_V \sim 22(0.44 \mathrm{pc}/D)^2$ and density of order $10^5(0.44 \, \mathrm{pc}/D)^3 \, \mathrm{cm^{-3}}$). The Bonner-Ebert critical mass for a gravitationally-bound clump, above which collapse of an unstable configuration occurs, is given by $M_\mathrm{crit}/\mathrm{M_\odot} \approx (D/\mathrm{pc})(T_\mathrm{gas}/\mathrm{K})$ (see e.g., Kerton et al. 2001, Equation 4). In these dense clumps, T_gas is probably close to the dust temperature and so for the derived T and M_c most of the clumps that we have identified would be unstable and are likely supported by additional pressure from turbulence or magnetic fields. On

release of this pressure, they have the potential to form a massive star or even a small cluster. Interestingly, several of the lowest mass clumps would be just stable if they were as extended as 1 pc.

The range of luminosities does indeed extend to $10^4\,L_\odot$ in NGC 6823, which corresponds to the luminosity of a B0.5 zero age main sequence star (Panagia 1973). But as we shall discuss further, at the low end, $\sim 40\,L_\odot$, there is by contrast no indication of significant star formation.

Luminosity as a function of mass is shown in Figures 18 and 19. This is essentially a reparameterization of the BLAST flux density vs. temperature plane, in terms of intrinsic source parameters. Because of the different distances for the two main groups, the Perseus arm sources and those associated with NGC 6823, the scaling of the axes is different, requiring similar but separate diagrams. Recall that the derived quantities are based on a SED fit assuming a modified blackbody SED with $\beta = 1.5$. Using this same model, the dotted lines are loci (with varying T) of constant $250\,\mu$m flux densities ranging from 10 to 1000 Jy. Orthogonal to these, the dashed lines are loci (with varying observed flux density) at constant $T = 10$, 20, 30, and 40 K. With our adopted model, these correspond to constant $L_{\rm FIR}/M_{\rm c}$, values of 0.07, 3.2, 30, and $140\,L_\odot\,M_\odot^{-1}$, respectively. The 11 objects with unreliable BLAST colors (§2.5, marked in Table 2) have been assigned a temperature of 20 K and so are seen distinctly along that locus. If these sources have different temperatures (probably lower given the usual lack of *IRAS* PSC counterparts), they would move along the constant flux density locus (down and right if cooler). These Figures can be used to investigate which early stages of star formation might be present. To this end, sources have been marked which lack *IRAS* PSC or *MSX* counterparts, or are UC H II regions

6.1. Mass Spectrum

The clumps that we have detected are much more massive than stars and therefore represent an early stage in star formation that is not easily, even empirically, related to the stellar initial mass function. Fragmentation and efficiency affect the transfer function in unknown ways. Nevertheless, it is interesting to investigate the mass spectrum, which we have done for the 49 BLAST sources associated with the NGC 6823 cloud complex. The
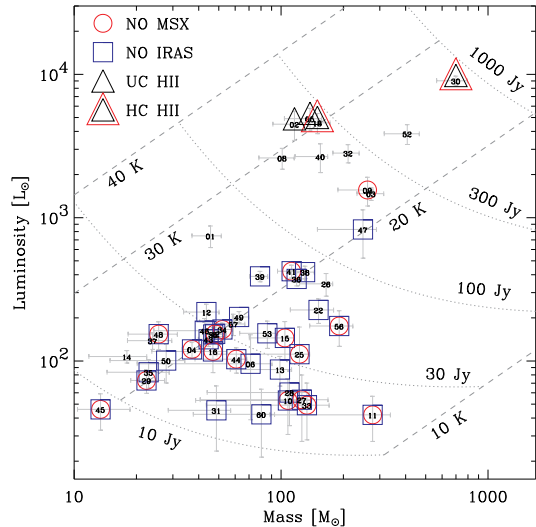
Fig. 18.— Luminosity vs. mass for the 49 objects believed to be associated with NGC 6823. Uncertainties in mass and luminosity are estimated from the range of temperatures consistent with the BLAST and FIR data under the assumption of the simple SED model of Equation 4. Not included are additional sources of error involving the distances to the objects and adopted values of β, κ_0, and gas-to-dust mass ratio. The dashed lines are loci at fixed temperatures (and $L_{\rm FIR}/M_{\rm c}$) of 10–40 K, assuming a modified blackbody SED with $\beta = 1.5$. Orthogonal to these are loci (dotted lines) of constant $250\,\mu$m flux density, ranging from 10 to 1000 Jy, using the same model. Sources lacking *IRAS* PSC or *MSX* counterparts are marked with circles and squares respectively. Ultra Compact H II region and Hyper Compact H II region candidates are indicated with single and double triangles, respectively.
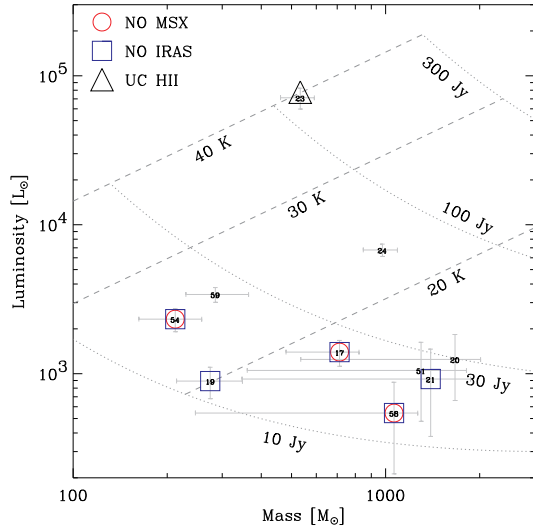
Fig. 19.— Same annotations as Figure 18, but for the 10 objects that are associated with the Perseus arm.

Fig. 20.— Mass function of the 49 objects associated with NGC 6823. Poisson error bars are shown, although there are additional sources of uncertainties for the parameters of Equation 5 for each object. For reference, the dashed line is a power-law, $150(M/50\,\mathrm{M_\odot})^{-1.7}$. The two lowest bins suggest a turnover, but this shape is probably due to incompleteness. To illustrate this the $250\,\mu$m flux density completeness (Figure 5) has been converted to a mass completeness using Equation 5 assuming various temperatures $T = 10$, 15, and 20 K. These are shown as dotted lines, arbitrarily scaled such that 100% completeness is 40 objects per bin.

masses of individual sources were placed in log-arithmically spaced bins (2 per decade); a lower limit on the error is then estimated from the Poisson uncertainty for each bin. The resulting mass function is shown in Figure 20.

At masses $\gtrsim 100\,\mathrm{M_\odot}$, the distribution is consistent with the mass functions of molecular clouds. For example, Kramer et al. (1998, and references therein) found a power-law index $\alpha \simeq 1.7$ in a mass range which encompasses the mass interval considered here. For reference, we have shown their power-law scaled vertically such that it passes through the high-mass bins in Figure 20: $dN/dM = 150(M/50\,\mathrm{M_\odot})^{-1.7}$. Note that adopting a different value of dust emissivity affects the inferred dust mass, since it is highly correlated with the fitted temperature (§4.2), and hence mass. For example, choosing $\beta = 2.0$ decreases temperatures by $\sim 5\,\mathrm{K}$, and increases cloud masses by a factor ~ 2. This effect shifts the mass function to the right in this figure, but does not affect the power-law index.

We note that the mass function in our sample appears to turn over at masses below $\sim 100\,\mathrm{M_\odot}$. However, the completeness of the survey also drops at these masses, with uncertainties that

25

are difficult to quantify given the range of object temperatures sampled (Figure 18). To attempt to assess the mass completeness, we converted the x-axis of the flux density completeness function (Figure 5) into mass using Equation 5, assuming consistently a distance of 2.3 kpc and $\kappa_0 = 10\,\mathrm{cm}^2\mathrm{g}^{-1}$. Some results are shown in Figure 20. If we assumed that the sources potentially missed had a temperature of 20 K, then completeness has a negligible effect, but for lower temperatures, which seem more probable, the effect is significant, because lower temperatures correspond to higher masses for a given flux density. See Johnstone et al. (2000) and Enoch et al. (2006) for further discussions regarding the completeness of mass spectrum estimates from submillimeter surveys. If, however, the turnover were real at $\sim 100\,\mathrm{M}_\odot$, our survey may be probing an interesting effect discussed by other authors (see Beltrán et al. 2006, and references therein). They claim that the point at which the mass distribution flattens is proportional to the mass range of clumps in star forming clouds.

7. DISCUSSION

7.1. Stages of Pre-stellar Evolution

This particular survey was not unbiased, since it targeted a region which has already formed massive stars and which contains bright *IRAS* sources which are protostar candidates. But it does fulfill one of the main goals of BLAST, to explore the sites of formation of high-mass stars and to examine the pre-stellar evolutionary sequence. In particular, with the BLAST wavebands we are sensitive to the earliest phases of massive star evolution, which would be molecular clumps lacking an internal energy source and thus cool with low $L_{\mathrm{FIR}}/M_\mathrm{c}$. In Figure 18 there are indeed many such low luminosity-to-mass ratio sources that are too faint and cool to have *IRAS* and *MSX* counterparts.

An interesting perspective is that the luminosity-to-mass ratio for diffuse cirrus in the local interstellar radiation field is of order $1\,\mathrm{L}_\od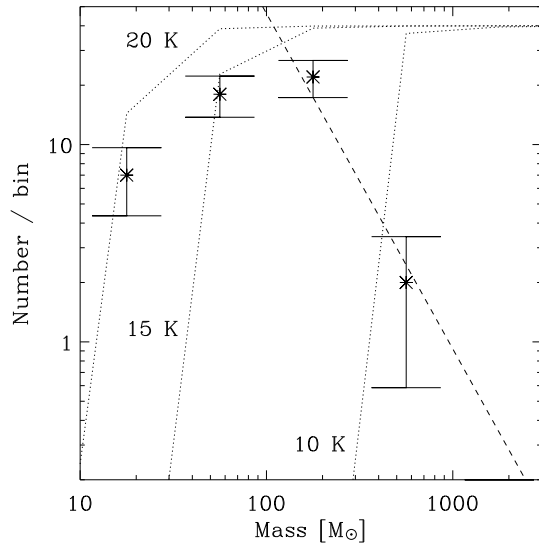ot\,\mathrm{M}_\odot^{-1}$. The low ratio (and lower temperature) found in these molecular clumps, even in the presence of a stronger impinging radiation field, is a result of the tremendous opacity to this external radiation, uncompensated by an internal source. In abso-

lute terms the luminosity of a cool clump can be quite impressive, because of the large mass, and yet not be a reliable indicator of there being star formation within.

Once a high-mass pre- or proto-stellar object begins to form, there is considerable luminosity to be reprocessed, resulting in higher $L_{\mathrm{FIR}}/M_\mathrm{c}$ and warmer dust. BLAST can of course see such objects as well, even those without MIR associations. There is not yet a unique definition or set of physical properties associated with HMPOs, but there is general agreement that they are heavily obscured objects (even making detection difficult in the MIR) that have not yet reached the stage at which the emergent Lyman continuum is sufficient to ionize the surrounding medium to form an H II region, and so they are undetected in the radio continuum as well. With spectral energy distributions peaking at wavelengths $\gtrsim 200\,\mu\mathrm{m}$ they can be extremely weak and undetectable by *IRAS* at $25\,\mu\mathrm{m}$, thus excluding them from previous surveys (e.g., Sridharan et al. 2002). Therefore the most unique BLAST objects, which are good HMPO candidates, are those with no *IRAS* or *MSX* counterparts, and no radio emission.

In the subsequent phase, when the massive protostar has become hotter, near the zero age main sequence, the ionizing capability is enhanced and a small region in the dense surroundings is ionized. Historically, such "ultra compact" (UC) H II regions have been the primary means to investigate the early phases of OB stellar evolution. This is a productive approach, since it deals with intrinsically luminous objects which are readily detectable, and the radio emission provides unequivocal evidence for an ionizing star. The more evolved, and therefore warmer, sources are more likely to have a MIR counterpart and be detectable by *MSX* and/or IRAC, than the colder and/or more deeply embedded sources. We do see such objects, as identified in Figures 18 and 19 (see §7.2).

In the past decade it has become clear that "hot-cores" represent a stage in the massive star formation process, probably somewhat earlier than UC H II regions (see, e.g., Kurtz et al. 2000, and references therein). The precise details of the transition are still lacking, and our understanding is complicated by the co-existence of objects at different evolutionary phases within the

same cluster. Also, the distinction between hot-cores and UC H II regions is often dependent on the sensitivity of the available observations, as several hot-cores are found to emit radio continuum emission if observed with enough sensitivity and angular resolution (opacity can also be a factor for dense objects). Likewise, although some authors list hot-cores as a subset of HMPOs (e.g., Sridharan et al. 2002), hot-cores are generally warmer, with $T_{\rm k} \gtrsim 100\,{\rm K}$, whereas objects called HMPOs usually have temperatures much lower than $100\,{\rm K}$ (e.g., Molinari et al. 1996). Also as noted by Sridharan et al. (2002), among higher luminosity objects, a low luminosity-to-mass ratio relative to that for UC H II regions might indicate a HMPO, though Beltrán et al. (2006) found no evidence to support this difference between their *"Low"* and *"High"* (less and more evolved) sources.

None of the objects that we detect has an inferred temperature greater than $40\,{\rm K}$ (assuming $\beta = 1.5$), even those that are UC H II regions. The temperature that we derive from the SED characterizes the bulk of the dust emission (more than 50 %) but of course is a simplification. When a protostar forms, the dust nearby is hotter than in the parent molecular clump, and also appears as a more compact source. Thus what is measured and interpreted as mass and luminosity depends on the radiative transfer and temperature gradient as well as the angular resolution of the measurements. While L reprocessed by dust (and the amount of ionization gauged from the radio continuum emission) are calorimeters for the embedded stellar population that is forming, the mass is that of the entire parent clump, depleted by accretion onto stars and later cloud dispersal. The luminosity-to-mass ratio can therefore be different, even for the same stellar population, being maximized for optical depth of order unity in a compact (and therefore warm) circumstellar region.

A plot like Figure 18 could be used to examine the evolutionary sequence, whether at constant $M_{\rm c}$ or otherwise, determining the lifetimes for each stage from the relative numbers of objects. However, this is complicated in practice by effects like clustering and detection bias and the fact that star formation does not proceed at precisely the same rate everywhere in a molecular clump. Thus with-

out adequate resolution it would be difficult to discriminate between material associated with an UC H II region and another nearby *cold* HMPO, for example. This problem can be remedied by high-resolution and high dynamic range observations (as anticipated with *Herschel* and ALMA); indeed in some cases interferometric observations have led to the detection of HMPOs in the same fields as the UC H II regions (see, e.g., Olmi et al. 2003, and references therein). Likewise, objects in Figure 18 with candidate *IRAS* and/or *MSX* counterparts, might in fact harbor a HMPO that is associated, but not coincident, with a MIR source at a later evolutionary stage in the same cluster.

7.2. Ultra Compact H II Regions

We have detected several *bona fide* UC H II regions, by which we mean compact objects whose bolometric luminosities *and* radio continuum emission are consistent with an embedded massive star near the zero age main sequence. Although within our beam there might be stars forming over a range of masses, the luminosity (and even more so the ionizing radiation), is dominated by the most massive and hottest stars with the earliest spectral types. Therefore, while not precise, it is still useful to characterize the region using a single spectral type. We use luminosities and ionizing rates from Panagia (1973), which to the accuracy required here are close to more modern values (Schaerer & de Koter 1997).

These sources can be been identified as UC H II *candidates* using color criteria based on *IRAS* measurements as in the Wood & Churchwell (1989), Kurtz et al. (1994), Bronfman et al. (1996) and Watson et al. (2003) catalogs (qualitatively, these sources are relatively weak at $12\,\mu{\rm m}$). Using the BLAST data we are able to find very accurate temperatures. Radio continuum measurements in the survey region at $1.4\,{\rm GHz}$ are available from the NRAO VLA Sky Survey (NVSS[4], Condon et al. 1998) and the VGPS (Stil et al. 2006). In addition, we searched the second and third MIT-Green Bank $5\,{\rm GHz}$ "MG" surveys (Langston et al. 1990; Griffith et al. 1990) which, though much shallower than NVSS, can provide a second flux density to estimate the spectral index between 1.4 and $5\,{\rm GHz}$. Some additional targeted obser-

---

[4]http://www.cv.nrao.edu/nvss/

vations at 4.9 GHz using Arecibo are described in Watson et al. (2003).

We will discuss these sources briefly in order of decreasing distance. V07 is the source in the outer Galaxy, which though fairly luminous ($3 \times 10^4\,\mathrm{L_\odot}$), is not among the more conspicuous sources in the maps. It is consistent with excitation (both luminosity and ionization) by a B0 star (only $20\,\mathrm{M_\odot}$ as compared to $600\,\mathrm{M_\odot}$ for the clump). In the VGPS radio image this source is extended and in the NVSS it is double. The second component, to lower longitude by about $1'$, coincides with a second *IRAS* source which appears at 12 and $25\,\mu$m.

V23, in the Perseus arm, is the most luminous source in this BLAST survey ($7 \times 10^4\,\mathrm{L_\odot}$; Figure 19), and a prominent radio, submillimeter, and infra-red source, despite its distance. Its excitation is consistent with a star as early as O7–8 ($30\,\mathrm{M_\odot}$, as compared to $500\,\mathrm{M_\odot}$ for the clump). The emission is extended, overlapping a second BLAST source V19, and is no doubt more complex than this simple description.

V02 and V05 are among the sources to which we have assigned the NGC 6823 distance (Figure 18). The luminosity implies a B2 zero age main sequence star, but the ionization (50 mJy radio continuum) requires B0.5 (for these relatively cool stars the ionization is extremely sensitive to the temperature). A further note is that the radio source, while being aligned with the *IRAS* source, is offset by $30''$ from V02.

V30, the brightest BLAST source and the most luminous source at this distance, is by contrast not an NVSS/VGPS source at 1.4 GHz. However, using the VLA B array at 8.2 GHz, Sridharan et al. (2002) found weak emission at the level of 1 mJy. Lower resolution Arecibo measurements at 4.9 GHz (Watson et al. 2003) give 3 mJy. Relative to V02 and V05, V30 is underluminous in the radio continuum by an order of magnitude. This could be because the central object, though luminous, has not become hot enough on approach to the zero age main sequence (it is a HMPO), or because of opacity if the surroundings of the protostar are very dense. We note that about 10% of the sources observed by Wood & Churchwell (1989) are optically thick at 2 cm, and a higher percentage may be applicable for the BLAST sources, since they probe the earliest stages of massive star formation. V30 might be

what is called a Hyper Compact (HC) H II region (e.g. Keto 2007), and has been marked accordingly in Figure 18.

The situation for the other comparably-luminous sources V08, V18, V32, and V52 is less clear. All but V18 meet the color criteria for being an UC H II region. However, none are NVSS sources. The detection of the V18 and V30 in targeted Arecibo observations (Watson et al. 2003) appears to be contradicted by the lower upper limits of 1 mJy with the VLA B array (Sridharan et al. 2002). This might suggest contamination of the Arecibo beam by diffuse continuum emission; as noted in §5.1, V32 is projected against the bright patchy Sh2-86 emission. On the other hand, V18 is coincident with a small ($20''$) cometary optical nebula and the Arecibo flux of 8 mJy might be the more relevant if the VLA resolved the extended emission. V18 may be another example of a HC H II region, and it is marked as a candidate in Figure 18. For V08 and V52 there are no sufficiently sensitive observations to isolate any weak emission, or alternatively, to qualify them as HMPOs.

Most of the radio sources in this survey region are not in fact associated with BLAST and *IRAS* sources (and vice versa). One must therefore be cautious of chance coincidences (for reference the surface density at the ~ 1 mJy level is $< 0.007\,\mathrm{arcmin^{-1}}$, Fomalont et al. 1991). There is a VGPS/NVSS source offset by $75''$ from V40 and its *IRAS* counterpart, also detected faintly at Arecibo (Watson et al. 2003). The level of radio emission is at least an order of magnitude greater than would be expected for the relatively low luminosity B2 star (Panagia 1973), so that it is probably not associated at all. Using the VLA B array at 8.2 GHz, Sridharan et al. (2002) placed a more definitive upper limit of 1 mJy. Note that such a HMPO will never become a significant H II region unless the stellar mass is increased through further accretion. There are NVSS sources near a few other even lower luminosity BLAST objects, V35, V39, V45, and V49 (and a marginal detection near V34). They are not detected in the shallower MG surveys and so no radio spectral index could be estimated. However, V35 has been detected in the Westerbork Synthesis Radio Telescope (WSRT) survey of Taylor et al. (1996). Its spectral index between 327 MHz and 1.4 GHz is

−1.6, and is therefore very unlikely to be associated with thermal emission. All of these sources are seen projected on Sh2-86, and so the radio "sources" could be just parts of the patchy ionization structure therein. As mentioned in §5, V39 is embedded at the end of a pillar adjacent to an ionization front caused by the exciting stars of NGC 6823, not V39. Inspection of the radio images suggests that V45 and V49 might be similarly confused.

Clearly, more sensitive radio observations, with spatial and spectral index information, are desirable to further elucidate the true nature of all of these (luminous) sources. But a firm conclusion that should be emphasized is that none of these BLAST sources associated with NGC 6823 reveal a protostar or HMPO more massive than a B0 to B1 star or about $20 \, \mathrm{M_\odot}$. There is thus no evidence for a new (or lagging) generation of stars that are as massive as the existing powerhouses of the NGC 6823 cluster, which reach about $40 \, \mathrm{M_\odot}$ (O7 V and O9.5 Ia; Schaerer & de Koter 1997).

7.3. Extended Submillimeter Emission

In this paper we have focused on the compact sources in the BLAST05 maps of Vulpecula. More diffuse structure could also be studied using algorithms such as CLUMPFIND (Williams et al. 1994). We leave such quantitative analysis for future work. However, it is worth illustrating a few features in the context of the discussion from §5.2 and the cool low luminosity-to-mass ratio clumps already identified.

Between sources V02 and V03 there is a pair of extended BLAST features, neither sufficiently compact to be included in our source catalog. The first, to the west of the line, is a strong $100 \mu m$ source, and even more prominent at $60 \mu m$; it is *IRAS* 19364+2252. This region exhibits a striking fan-shaped nebulosity in the IRAC $8 \, \mu m$ map (Figure 17). Since the object is also a radio source, it is probably an evolved object. It has weak emission in the BLAST maps and is anti-coincident with ^{13}CO. The second source, right on the line, is possibly related to the *IRAS* source 19367+2251, which IGA/MIGA show to be much weaker as a compact source than the first. This extended BLAST source coincides with a peak in ^{13}CO and becomes brighter relative to the first source at increasing BLAST wavelengths. This behavior implies that it is a very cold object.

Another example is associated with the pair of *IRAS* sources 19385+2245 and 19389+2233. They can be seen in all of the *IRAS* bands, but they are both diffuse in the BLAST maps. The first is weak in ^{13}CO and has complex structure in the $8 \, \mu m$ map. The second is elongated in BLAST and has a strong elongated CO cloud as well. It is also extended at $8 \, \mu m$, with a slight offset from the submillimeter source.

A future analysis of such cold clouds in BLAST maps in conjunction with MIPS and IRAC source catalogs may be used to determine whether they represent an even earlier phase before condensations form, or if they are simply distant cold envelopes of established young stellar objects.

8. CONCLUSIONS

In this paper we present the first maps of the Galactic Plane observed with BLAST during its 2005 LDB flight from Sweden to Canada, specifically the survey in the direction of star forming clouds in Vulpecula.

Fourier deconvolution is used to improve the angular resolution of the maps from ~ 3.5 to $\sim 1'$ full-width half-power (the theoretical $500 \, \mu m$ diffraction limit). In these maps, 60 compact submillimeter sources are detected simultaneously at 250, 350, and $500 \, \mu m$. Complementary *IRAS*, MIPSGAL, and *MSX* photometry are used to constrain the submillimeter-MIR SEDs of these objects, and hence infer their cold dust temperatures and bolometric fluxes. Our sample has convincingly revealed objects with a range of dust temperatures, from ~ 12–40 K under the assumption of an isothermal modified blackbody with dust emissivity index $\beta = 1.5$. With these SED fits, we derive luminosity-to-mass ratios (independent of distance) in the range 0.2–$130 \, \mathrm{L_\odot \, M_\odot^{-1}}$. Those with low values are highly shielded and cool, with no evidence for star formation, while those with high values have embedded high-mass star formation.

Using a ^{13}CO(1 → 0) data cube, the VLA Galactic Plane Survey H I cube, *Spitzer* IRAC and optical DSS images, we argue that 49 of the 60 sources lie in a molecular cloud complex associated with the open cluster NGC 6823 at $\sim 2.3 \, \mathrm{kpc}$, 10 objects are associated with the Perseus arm at $\sim 8.5 \, \mathrm{kpc}$ and 1 object is in the outer Galaxy at

$\sim 14\,\mathrm{kpc}$. With these distance estimates we calculate bolometric luminosities and cloud masses associated with the thermal emission from cold dust. The most luminous object $(7 \times 10^4\,\mathrm{L}_\odot)$ is in the Perseus arm. Near NGC 6823, the ranges are ~ 40–$10^4\,\mathrm{L}_\odot$, and ~ 15–$700\,\mathrm{M}_\odot$.

A mass function is constructed for the 49 objects associated with NGC 6823. It is compatible with the spectrum of molecular gas masses in other high-mass star forming regions, with a power-law index of -1.7 for the $\gtrsim 100\,\mathrm{M}_\odot$ sources. A flattening at lower masses might be present, but is affected by detection completeness of cool sources in this mass range.

The luminosity-mass distribution we find is broadly consistent with an evolutionary sequence, from cool high-mass, low-luminosity clumps (most are not detected with *IRAS* or *MSX* and there is no evidence for any star formation), to more evolved HMPOs and UC H II regions. But interestingly, among the embedded objects in this molecular complex near NGC 6823 – the next generation – there are none quite as massive as the $40\,\mathrm{M}_\odot$ stars currently powering the nebula.

REFERENCES

Aumann, H. H., Fowler, J. W., & Melnyk, M. 1990, AJ, 99, 1674

Barnard, V. E., Vielva, P., Pierce-Price, D. P. I., Blain, A. W., Barreiro, R. B., Richer, J. S., & Qualtrough, C. 2004, MNRAS, 352, 961

Beltrán, M. T., Brand, J., Cesaroni, R., Fontani, F., Pezzuto, S., Testi, L., & Molinari, S. 2006, A&A, 447, 221

Beuther, H., Schilke, P., Menten, K. M., Motte, F., Sridharan, T. K., & Wyrowski, F. 2002, ApJ, 566, 945

Brand, J. & Blitz, L. 1993, A&A, 275, 67

Bronfman, L., Nyman, L.-A., & May, J. 1996, A&AS, 115, 81

Brunt, C. M. & Heyer, M. H. 2007, in prep.

Cao, Y., Terebey, S., Prince, T. A., & Beichman, C. A. 1997, ApJS, 111, 387

Carey, S. J., Noriega-Crespo, A., Price, S. D., Padgett, D. L., Kraemer, K. E., Indebetouw, R., Mizuno, D. R., Ali, B., Berriman, G. B., Boulanger, F., Cutri, R. M., Ingalls, J. G., Kuchar, T. A., Latter, W. B., Marleau, F. R., Miville-Deschenes, M. A., Molinari, S., Rebull, L. M., & Testi, L. 2005, in Bulletin of the American Astronomical Society, 1252–+

Condon, J. J., Cotton, W. D., Greisen, E. W., Yin, Q. F., Perley, R. A., Taylor, G. B., & Broderick, J. J. 1998, AJ, 115, 1693

Dupac, X., Giard, M., Bernard, J.-P., Lamarre, J.-M., Mény, C., Pajot, F., Ristorcelli, I., Serra, G., & Torre, J.-P. 2001, ApJ, 553, 604

Egan, M. P., Price, S. D., Kraemer, K. E., Mizuno, D. R., Carey, S. J., Wright, C. O., Engelke, C. W., Cohen, M., & Gugliotti, M. G. 2003, VizieR Online Data Catalog, 5114, 0

Egan, M. P., Shipman, R. F., Price, S. D., Carey, S. J., Clark, F. O., & Cohen, M. 1998, ApJ, 494, L199+

Enoch, M. L., Glenn, J., Evans, II, N. J., Sargent, A. I., Young, K. E., & Huard, T. L. 2007, ArXiv e-prints, 705

Enoch, M. L., Young, K. E., Glenn, J., Evans, II, N. J., Golwala, S., Sargent, A. I., Harvey, P., Aguirre, J., Goldin, A., Haig, D., Huard, T. L., Lange, A., Laurent, G., Maloney, P., Mauskopf, P., Rossinot, P., & Sayers, J. 2006, ApJ, 638, 293

Fomalont, E. B., Windhorst, R. A., Kristian, J. A., & Kellerman, K. I. 1991, AJ, 102, 1258

Gibson, S. J., Taylor, A. R., Higgs, L. A., & Dewdney, P. E. 2000, ApJ, 540, 851

Griffin, M. J., Swinyard, B. M., & Vigroux, L. G. 2003, in Presented at the Society of Photo-Optical Instrumentation Engineers (SPIE) Conference, Vol. 4850, IR Space Telescopes and Instruments. Edited by John C. Mather . Proceedings of the SPIE, Volume 4850, pp. 686-697 (2003)., ed. J. C. Mather, 686–697

Griffith, M., Langston, G., Heflin, M., Conner, S., Lehar, J., & Burke, B. 1990, ApJS, 74, 129

Guetter, H. H. 1992, AJ, 103, 197

Helou, G. & Walker, D. W., eds. 1988, Infrared astronomical satellite (IRAS) catalogs and atlases. Volume 7: The small scale structure catalog, Vol. 7

Hildebrand, R. H. 1983, QJRAS, 24, 267

Hill, T., Thompson, M. A., Burton, M. G., Walsh, A. J., Minier, V., Cunningham, M. R., & Pierce-Price, D. 2006, MNRAS, 368, 1223

Holland, W. S., Robson, E. I., Gear, W. K., Cunningham, C. R., Lightfoot, J. F., Jenness, T., Ivison, R. J., Stevens, J. A., Ade, P. A. R., Griffin, M. J., Duncan, W. D., Murphy, J. A., & Naylor, D. A. 1999, MNRAS, 303, 659

Hoyle, F., Shanks, T., & Tanvir, N. R. 2003, MNRAS, 345, 269

Isobe, T., Feigelson, E. D., & Nelson, P. I. 1986, ApJ, 306, 490

Johnstone, D., Wilson, C. D., Moriarty-Schieven, G., Joncas, G., Smith, G., Gregersen, E., & Fich, M. 2000, ApJ, 545, 327

Kerton, C. R. & Martin, P. G. 2000, ApJS, 126, 85

Kerton, C. R., Martin, P. G., Johnstone, D., & Ballantyne, D. R. 2001, ApJ, 552, 601

Keto, E. 2007, ApJ, 666, 976

Kharchenko, N. V., Piskunov, A. E., Röser, S., Schilbach, E., & Scholz, R.-D. 2005, A&A, 438, 1163

Kirk, J. M., Ward-Thompson, D., & André, P. 2005, MNRAS, 360, 1506

Kramer, C., Stutzki, J., Rohrig, R., & Corneliussen, U. 1998, A&A, 329, 249

Kreysa, E., Gemuend, H.-P., Gromke, J., Haslam, C. G., Reichertz, L., Haller, E. E., Beeman, J. W., Hansen, V., Sievers, A., & Zylka, R. 1998, in Proc. SPIE Vol. 3357, p. 319-325, Advanced Technology MMW, Radio, and Terahertz Telescopes, Thomas G. Phillips; Ed., ed. T. G. Phillips, 319–325

Kuchar, T. A. & Bania, T. M. 1994, ApJ, 436, 117

Kurtz, S., Cesaroni, R., Churchwell, E., Hofner, P., & Walmsley, C. M. 2000, Protostars and Planets IV, 299

Kurtz, S., Churchwell, E., & Wood, D. O. S. 1994, ApJS, 91, 659

Langston, G. I., Heflin, M. B., Conner, S. R., Lehar, J., Carrilli, C. L., & Burke, B. F. 1990, ApJS, 72, 621

Lockman, F. J. 1989, ApJS, 71, 469

Massey, P., Johnson, K. E., & Degioia-Eastwood, K. 1995, ApJ, 454, 151

Menten, K. 2007, in Massive Star Formation: Observations confront Theory, ed. H. Beuther

Miville-Deschênes, M.-A. & Lagache, G. 2005, ApJS, 157, 302

Molinari, S., Brand, J., Cesaroni, R., & Palla, F. 1996, A&A, 308, 573

Moore, T. T., Bretherton, D., Fujiyoshi, T., Ridge, N., Allsopp, J., Hoare, M., Lumsden, S., & Richer, J. 2007, ArXiv e-prints, 705

Motte, F., Bontemps, S., Schilke, P., Schneider, N., Menten, K. M., & Broguière, D. 2007, ArXiv e-prints, 708

Olmi, L., Cesaroni, R., Hofner, P., Kurtz, S., Churchwell, E., & Walmsley, C. M. 2003, A&A, 407, 225

Ossenkopf, V. & Henning, T. 1994, A&A, 291, 943

Panagia, N. 1973, AJ, 78, 929

Pascale, E. et al. 2007, ApJ, submitted

Patanchon, G. et al. 2007, ApJ, submitted

Peña, J. H., García-Cole, A., Hobart, M. A., de La Cruz, C., Plascencia, J. C., & Peniche, R. 2003, Revista Mexicana de Astronomia y Astrofisica, 39, 171

Pierce-Price, D., Richer, J. S., Greaves, J. S., Holland, W. S., Jenness, T., Lasenby, A. N., White, G. J., Matthews, H. E., Ward-Thompson, D., Dent, W. R. F., Zylka, R., Mezger, P., Hasegawa, T., Oka, T., Omont, A., & Gilmore, G. 2000, ApJ, 545, L121

Rathborne, J. M., Shah, R. Y., Jackson, J. M., R. Y., Bania, T. M., Clemens, D. P., Johnson, A. M., Flynn, E., Bonaventura, N., Simon, R., & Meyer, M. H. 2004, in Milky Way Surveys: The Structure and Evolution of our Galaxy

Reid, M. A. & Wilson, C. D. 2005, ApJ, 625, 891

Schaerer, D. & de Koter, A. 1997, A&A, 322, 598

Schlegel, D. J., Finkbeiner, D. P., & Davis, M. 1998, ApJ, 500, 525

Schneider, N., Bontemps, S., Simon, R., Jakob, H., Motte, F., Miller, M., Kramer, C., & Stutzki, J. 2006, A&A, 458, 855

Simon, R., Rathborne, J. M., Shah, R. Y., Jackson, J. M., & Chambers, E. T. 2006, ApJ, 653, 1325

Sridharan, T. K., Beuther, H., Schilke, P., Menten, K. M., & Wyrowski, F. 2002, ApJ, 566, 931

Starck, J. L., Pantin, E., & Murtagh, F. 2002, PASP, 114, 1051

Stil, J. M., Taylor, A. R., Dickey, J. M., Kavars, D. W., Martin, P. G., Rothwell, T. A., Boothroyd, A. I., Lockman, F. J., & McClure-Griffiths, N. M. 2006, AJ, 132, 1158

Szymczak, M., Hrynek, G., & Kus, A. J. 2000, A&AS, 143, 269

Taylor, A. R., Goss, W. M., Coleman, P. H., van Leeuwen, J., & Wallace, B. J. 1996, ApJS, 107, 239

Taylor, A. R., Wallace, B. J., & Goss, W. M. 1992, AJ, 103, 931

Taylor, J. H. & Cordes, J. M. 1993, ApJ, 411, 674

Thompson, M. A., Gibb, A. G., Hatchell, J. H., Wyrowski, F., & Pillai, T. 2005, in The Dusty and Molecular Universe: A Prelude to Herschel and ALMA, ed. A. Wilson, 425–426

Thompson, M. A., Hatchell, J., Walsh, A. J., Mac-Donald, G. H., & Millar, T. J. 2006, A&A, 453, 1003

Truch, M. et al. 2007, ApJ, submitted

Turner, A. D., Bock, J. J., Beeman, J. W., Glenn, J., Hargrave, P. C., Hristov, V. V., Nguyen, H. T., Rahman, F., Sethuraman, S., & Woodcraft, A. L. 2001, Appl. Opt., 40, 4921

Watson, C., Araya, E., Sewilo, M., Churchwell, E., Hofner, P., & Kurtz, S. 2003, ApJ, 587, 714

Whitney, B. A. & GLIMPSE Team. 2005, in Bulletin of the American Astronomical Society, Vol. 37, Bulletin of the American Astronomical Society, 1323–+

Williams, J. P., de Geus, E. J., & Blitz, L. 1994, ApJ, 428, 693

Wood, D. O. S. & Churchwell, E. 1989, ApJS, 69, 831

Young, K. E., Enoch, M. L., Evans, II, N. J., Glenn, J., Sargent, A., Huard, T. L., Aguirre, J., Golwala, S., Haig, D., Harvey, P., Laurent, G., Mauskopf, P., & Sayers, J. 2006, ApJ, 644, 326

Zhang, Q., Hunter, T. R., Brand, J., Sridharan, T. K., Cesaroni, R., Molinari, S., Wang, J., & Kramer, M. 2005, ApJ, 625, 864

Zinchenko, I., Henning, T., & Schreyer, K. 1997, A&AS, 124, 385

TABLE 2
BLAST SOURCES

BLAST ID	Source name	F_{250} (Jy)	σ_{250} (Jy)	F_{350} (Jy)	σ_{350} (Jy)	F_{500} (Jy)	σ_{500} (Jy)	V_{lsr} km s^{-1}
V01	BLAST J193837+230541	59.9	4.2	27.1	2.8	11.0	1.2	30.8
V02	BLAST J193849+230839	258.0	5.1	97.8	3.4	36.9	1.3	32.3
V03	BLAST J193858+224637	197.9	4.7	101.9	3.5	44.5	1.3	36.5
V04[a]	BLAST J193921+224401	23.6	4.1	8.9	2.7	7.3	1.2	27.3
V05	BLAST J193935+235947	325.7	5.6	124.1	3.8	43.6	1.3	37.0
V06	BLAST J193943+232601	20.4	4.1	13.1	2.7	5.8	1.2	43.2
V07[b]	BLAST J194046+241007	38.7	4.1	12.2	2.7	5.2	1.1	−53.5
V08	BLAST J194059+240439	225.6	4.9	81.6	3.2	30.7	1.2	34.8
V09	BLAST J194103+240111	194.8	4.7	102.1	3.5	41.2	1.3	34.4
V10	BLAST J194106+235513	21.5	4.1	12.6	2.7	6.7	1.2	34.0
V11	BLAST J194136+232325	18.3	4.0	18.9	2.7	10.1	1.2	27.8
V12	BLAST J194144+231410	33.2	4.1	16.9	2.7	7.1	1.1	29.4
V13	BLAST J194144+231804	26.6	4.1	16.4	2.7	7.5	1.2	23.7
V14	BLAST J194146+234914	19.0	4.1	10.3	2.7	3.3	1.1	34.6
V15	BLAST J194213+232305	41.9	4.1	21.8	2.7	10.5	1.2	24.6
V16	BLAST J194217+231958	23.5	4.1	10.8	2.7	5.5	1.2	33.0
V17[c]	BLAST J194226+234532	30.4	4.1	10.8	2.7	5.6	1.2	−2.1
V18	BLAST J194228+230458	259.9	5.1	114.3	3.6	42.8	1.3	26.6
V19[ac]	BLAST J194232+234913	15.8	4.1	5.6	2.7	2.2	1.1	-3.0
V20[c]	BLAST J194232+234253	27.6	4.1	17.9	2.7	9.3	1.2	0.8
V21[c]	BLAST J194234+234412	20.9	4.1	15.6	2.7	6.6	1.2	−0.3
V22	BLAST J194234+232321	60.9	4.1	34.8	2.8	15.1	1.2	30.5
V23[c]	BLAST J194236+235003	129.6	4.4	45.8	2.9	15.7	1.2	-3.0
V24[c]	BLAST J194244+234021	62.5	4.2	37.1	2.8	12.3	1.2	0.3
V25	BLAST J194246+225536	30.1	4.1	17.7	2.7	10.3	1.2	26.9
V26	BLAST J194254+232408	73.2	4.2	42.4	2.8	18.8	1.2	31.4
V27	BLAST J194306+230125	19.8	4.1	14.1	2.7	7.0	1.2	27.0
V28	BLAST J194308+232457	21.0	4.1	15.0	2.7	6.5	1.2	33.1
V29[a]	BLAST J194311+232010	15.7	4.1	2.3	2.7	5.5	1.2	24.0
V30	BLAST J194311+234405	852.7	11.0	378.5	8.5	153.4	2.7	22.8
V31	BLAST J194311+232237	13.3	4.1	19.1	2.7	2.3	1.1	33.4
V32	BLAST J194317+231352	221.2	4.9	110.7	3.6	43.3	1.3	29.3
V33	BLAST J194319+232639	17.5	4.0	17.7	2.7	6.7	1.2	22.5
V34[a]	BLAST J194319+233906	27.5	4.1	24.1	2.7	7.4	1.2	22.9
V35	BLAST J194323+231512	22.0	4.1	7.9	2.7	1.4	1.1	30.4
V36[a]	BLAST J194325+234503	86.6	4.2	68.3	3.1	18.9	1.2	21.3
V37	BLAST J194326+240618	24.8	4.1	9.3	2.7	3.5	1.1	20.7
V38[a]	BLAST J194327+235638	64.4	4.2	43.8	2.9	22.6	1.2	22.4[d]
V39	BLAST J194328+232032	57.8	4.1	31.1	2.8	12.6	1.2	25.7
V40	BLAST J194329+234013	189.7	4.7	86.9	3.3	35.4	1.3	20.5
V41	BLAST J194331+235728	90.8	4.2	42.7	2.8	16.3	1.2	22.8
V42[a]	BLAST J194333+231445	23.8	4.1	24.0	2.7	7.5	1.2	26.9
V43[a]	BLAST J194334+232737	41.8	4.1	24.7	2.8	3.6	1.1	26.9
V44	BLAST J194335+235332	28.2	4.1	14.7	2.7	5.5	1.2	21.4

Zinnecker, H. & Yorke, H. W. 2007, ARA&A, 45, 481

TABLE 2—*Continued*

BLAST ID	Source name	F_{250} (Jy)	σ_{250} (Jy)	F_{350} (Jy)	σ_{350} (Jy)	F_{500} (Jy)	σ_{500} (Jy)	V_{lsr} km s^{-1}
V45[a]	BLAST J194338+231725	10.6	4.1	7.0	2.7	0.4	1.1	26.6
V46	BLAST J194340+235506	28.8	4.1	12.5	2.7	5.3	1.1	22.5
V47	BLAST J194342+232006	129.9	4.4	70.2	3.1	33.8	1.3	26.7
V48	BLAST J194344+240005	23.5	4.1	11.2	2.7	3.3	1.1	22.2
V49[a]	BLAST J194346+232532	27.0	4.1	17.9	2.7	11.5	1.2	26.1
V50	BLAST J194347+233505	18.6	4.1	10.1	2.7	3.0	1.1	22.1
V51[c]	BLAST J194349+230840	22.4	4.1	16.1	2.7	6.8	1.2	-7.0
V52	BLAST J194350+232839	486.4	7.1	214.5	5.3	84.2	1.8	27.6
V53	BLAST J194350+231846	40.6	4.1	20.0	2.7	9.1	1.2	27.7
V54[c]	BLAST J194351+234625	21.8	4.1	7.0	2.7	2.4	1.1	3.2[e]
V55[a]	BLAST J194402+232409	30.6	4.1	21.9	2.7	5.0	1.2	29.3
V56	BLAST J194404+234418	53.5	4.1	37.3	2.8	15.6	1.2	21.7
V57	BLAST J194405+232658	40.7	4.1	19.6	2.7	7.1	1.2	27.2
V58[c]	BLAST J194409+230437	15.4	4.1	10.7	2.7	5.2	1.2	-12.7
V59[c]	BLAST J194424+234239	23.8	4.1	12.9	2.7	4.1	1.1	-10.7
V60	BLAST J194430+233426	14.9	4.1	14.1	2.7	4.8	1.2	26.2

NOTE.—Flux densities for BLAST sources are quoted at precisely 250, 350, and 500 μm using SED fits to obtain color-corrections for the band-averaged flux densities (§4). The quoted statistical uncertainties are determined from Monte Carlo simulations (§2.6), and do not include calibration uncertainties.

[a]These sources are located on ripples in the deconvolved map and the BLAST colors are considered unreliable as a result.

[b]V07 is believed to lie in the outer galaxy.

[c]These sources are associated with a molecular cloud in the Perseus arm.

[d]Also has a comparable component at $-15\,\mathrm{km\,s^{-1}}$.

[e]Also has a comparable component at $23\,\mathrm{km\,s^{-1}}$.

TABLE 3
IRAS PSC COUNTERPARTS

BLAST ID	IRAS ID	$\Delta\alpha^a$ ($''$)	$\Delta\delta^a$ ($''$)	F_{12} (Jy)	F_{25} (Jy)	F_{60} (Jy)	F_{100} (Jy)
V01	19364+2258	−19.4	−3.3	0.8	8.3	389.0^b	698.0^b
V02	19366+2301	−21.0	−1.0	8.8	62.0	389.0	698.0
V03	19368+2239	−4.5	−5.4	2.3	11.7	112.0	231.0
V05	19374+2352	−27.0	7.3	4.6	24.3	422.0	768.0
V07	19386+2403	−5.9	2.1	1.8	4.7	71.2	63.8
V08	19388+2357	−3.0	−0.1	1.3	10.9	254.0	433.0
V09	19389+2354	1.5	−0.1	1.8	1.2^b	58.2	433.0^b
V14	19396+2342	3.1	9.6	1.5^b	0.8^b	3.1	16.7
V18	19403+2258	−21.0	13.9	16.2	118.0	562.0	640.0
V20	19404+2335	−6.0	0.2	1.9^b	1.0	4.9^b	53.0^b
V23^c	19404+2342	−24.0	−7.9	9.7	35.3	439.0	980.0
V24	19406+2333	0.0	8.1	0.7	5.1	35.0	89.8
V26	19407+2316	−4.5	−6.8	4.1^b	4.2	23.2	165.0^b
V30	19410+2336	4.5	0.9	14.4	109.0	982.0	1630.0
V32	19411+2306	12.0	6.2	5.3	41.2	159.0	557.0
V37	19413+2358	−3.0	−8.7	15.4^b	0.8^b	4.5	37.0^b
V38^d	19413+2349	10.5	20.1	0.7	4.6	42.5	132.0
V40	19413+2332	−4.5	−9.3	4.2	38.5	217.0	1630.0^b
V51	19416+2301	0.0	−12.9	1.0^b	1.0	4.7^b	35.8^b
V52	19416+2321	−18.0	20.5	5.0^b	24.7^b	268.0	624.0
V53^d	19416+2312	−39.0	39.3	0.6	10.7^b	13.6^b	250.0
V57	19419+2319	4.5	−15.0	2.8	2.6	36.1^b	624.0^b
V59	19422+2335	−1.5	2.1	1.4	2.3	25.6	46.6

NOTE.—*IRAS* point sources associated with BLAST objects. The search radius is a variable function of both BLAST and *IRAS* positional uncertainties (see §3.1).

^{a}BLAST source tangent plane offsets (E and N) compared to *IRAS* source position.

^{b}These *IRAS* measurements are flagged as upper-limits in the catalog (usually due to confusion). Values from Table 4 are used instead.

^{c}IRAS 19404+2342 is close to both V19 and V23; the ambiguity is resolved with the improved resolution of the MIPS 70 μm map.

^{d}Although IRAS 19413+2349 and 19416+2312 are close to V38 and V53 respectively, their SEDs are not compatible with the BLAST photometry and the identifications are not used in subsequent analyses.

TABLE 4
IRAS AND *Spitzer* MIPS PHOTOMETRY

BLAST ID	F_{12} (Jy)	Flag	F_{25} (Jy)	Flag	F_{60} (Jy)	Flag	F_{100} (Jy)	Flag	F_{70} (Jy)	Flag
V01	1.2[a]	g	7.2[a]	g	46.5	g	120.5	u	33.0	s
V02	12.1[a]	g	60.9[a]	g	437.7[a]	g	733.6[a]	g	211.1	s
V03	2.4[a]	g	12.4[a]	g	114.5[a]	g	243.2[a]	g	78.2	s
V04	0.2	n	0.2	n	0.2	n	31.3	n	0.4	n
V05	5.9[a]	g	28.6[a]	g	410.5[a]	g	772.9[a]	g	218.6	s
V06	−0.1	n	−0.1	n	4.2	g	24.7	u	2.5	g
V07	1.7[a]	g	4.7[a]	g	66.7[a]	g	135.7[a]	g	50.4	s
V08	2.3[a]	g	12.1[a]	g	259.9[a]	g	569.6[a]	g	206.7	s
V09	1.5[a]	g	2.9	g	44.1[a]	g	256.8	u	44.1	s
V10	0.0	n	0.0	g	2.4	u	48.3	u	0.9	n
V11	−0.1	n	−0.2	n	−0.2	n	18.2	n	0.8	n
V12	1.7	g	4.0	g	14.8	g	70.9	u	9.4	g
V13	−0.4	n	−0.4	n	−3.6	n	13.0	n	−1.5	n
V14	0.3	n	0.5	u	4.0[a]	g	28.0[a]	u	2.7	g
V15	−0.2	n	0.2	n	9.4	u	83.3	u	3.1	n
V16	1.2	u	2.0	n	11.7	u	91.9	u	3.5	g
V17	0.2	n	0.9	u	5.9	u	14.5	n	3.4	n
V18	17.2[a]	g	108.5[a]	g	570.0[a]	g	699.1[a]	g	275.4	s
V19	17.6	u	52.8	u	460.1	u	979.5	u	148.6	s
V20	0.0	g	0.3[a]	g	6.6	u	19.4	n	6.3	g
V21	−0.1	n	−0.3	n	−1.9	n	−0.1	n	4.5	g
V22	0.7	n	0.5	n	7.4	u	97.7	u	6.0	n
V23	15.3[a]	u	53.3[a]	u	506.5[a]	g	916.8[a]	g	192.2	s
V24	1.4[a]	u	3.5[a]	g	32.0[a]	g	110.6[a]	u	25.5	s
V25	0.2	n	0.9	u	3.8	g	47.0	g	0.7	g
V26	2.0	u	4.0[a]	g	21.9[a]	g	91.4	u	7.7	g
V27	0.4	u	0.7	u	7.7	u	51.7	u	0.7	n
V28	2.6	u	4.2	u	−3.3	n	36.9	n	3.2	n
V29	−0.7	n	0.1	n	−0.5	n	−6.2	n	−0.9	g
V30	18.5[a]	g	118.0[a]	g	892.2[a]	g	1463.9[a]	g	378.2	s
V31	0.7	n	0.9	u	2.0	n	−7.8	n	−0.3	n
V32	6.1[a]	g	37.3[a]	g	151.2[a]	g	478.2[a]	g	62.6	s
V33	1.2	n	1.9	u	21.5	u	37.0	u	−1.3	n
V34	3.2	u	5.4	u	83.9	u	334.1	u	2.2	n
V35	6.2	u	22.9	u	87.9	u	461.9	u	6.6	n
V36	5.6	u	8.6	g	88.4	u	472.2	u	42.6	s
V37	0.3	n	0.8	n	4.4[a]	g	24.6	u	3.3	g
V38	0.9	u	5.3	u	34.0	u	120.9	u	22.9	s
V39	3.8	u	3.7	g	40.4	u	183.2	u	19.4	g
V40	7.2[a]	g	44.4[a]	g	214.3[a]	g	400.5	g	152.3	s
V41	0.6	n	5.2	u	33.5	u	131.7	u	17.8	u
V42	−0.8	n	−0.6	n	−0.6	n	223.5	u	−3.3	n
V43	1.8	n	1.6	n	21.1	u	147.6	u	7.8	n
V44	0.0	n	0.1	n	3.6	u	35.2	n	2.0	u

TABLE 4—*Continued*

BLAST ID	F_{12} (Jy)	Flag	F_{25} (Jy)	Flag	F_{60} (Jy)	Flag	F_{100} (Jy)	Flag	F_{70} (Jy)	Flag
V45	0.0	n	3.9	u	1.7	n	17.7	n	6.8	n
V46	0.0	n	−0.2	n	9.5	u	137.3	u	12.3	u
V47	0.9	g	10.5	g	60.5	g	174.6	g	21.0	s
V48	0.8	n	1.2	n	9.0	u	61.0	u	8.2	g
V49	−0.9	n	1.0	n	16.7	u	149.0	u	17.6	g
V50	0.2	g	1.0	g	6.7	u	51.5	u	4.2	g
V51	0.3	n	1.9[a]	n	15.9	u	103.5	u	3.2	g
V52	4.4	u	27.6	u	278.2[a]	g	675.1[a]	g	211.7	s
V53	−0.5[a]	n	−0.3	n	5.5	n	227.9[a]	u	0.7	n
V54	0.5	u	0.9	u	11.2	u	82.4	u	12.9	g
V55	1.9	u	5.6	u	11.3	g	369.6	u	8.1	n
V56	−0.1	n	−0.3	n	1.1	n	31.4	u	−0.4	n
V57	1.7[a]	g	5.3[a]	g	4.5	n	423.2	u	5.7	g
V58	−0.1	n	−0.2	n	7.2	u	90.1	u	2.5	g
V59	1.4[a]	g	2.3[a]	g	26.4[a]	g	57.4[a]	g	24.7	s
V60	0.8	n	1.3	u	10.6	u	75.4	u	2.2	n

NOTE.—*IRAS* and *Spitzer* MIPS map photometry are described in §3.1 and §3.2 respectively. Each measurement is flagged upon visual inspection: "g" if it is good; "u" for upper limit; "n" for no visible source; and "s" for saturated (unreliable) values in the MIPS 70 μm map.

[a]Clear detections from the *IRAS* PSC (Table 3) are used in favor of these values when available.

TABLE 5
MSX counterparts

BLAST ID	$\Delta\alpha^{\mathrm{a}}$ (″)	$\Delta\delta^{\mathrm{a}}$ (″)	$F_8.3$ (Jy)	$F_{12.1}$ (Jy)	$F_{14.7}$ (Jy)	$F_{21.3}$ (Jy)
V01	−6.9	1.4	0.9	0.8	0.8	4.7
V02	−11.0	−1.3	4.3	5.3	3.7	23.9
V03	18.0	8.1	0.9	1.1	0.6	1.6
	−20.7	−9.9	0.8	1.0	1.4	3.4
V05	−6.9	26.0	1.7	1.8	1.2	2.7
	−2.7	2.9	0.9	0.8	1.2	6.2
V06	19.3	−63.1	0.4	⋯	⋯	⋯
V07	−0.0	11.2	1.0	1.4	0.8	2.0
	−26.0	−53.6	0.1	1.2	⋯	⋯
V08	−0.0	−23.9	0.6	1.4	0.9	⋯
	−8.2	6.7	0.5	1.3	0.8	3.6
V12	−48.2	−41.7	1.7	1.2	0.7	⋯
	8.3	9.8	0.5	2.0	3.1	4.7
V13	−4.1	21.1	0.1	⋯	⋯	⋯
V14	−11.0	16.7	0.2	⋯	0.8	⋯
V18	−8.3	16.9	8.4	9.0	6.2	57.5
V19	11.0	28.5	0.9	1.8	2.2	3.9
	37.0	38.2	0.7	2.6	3.2	7.9
	−9.6	49.0	0.1	0.6	⋯	1.3
V20	−0.0	−0.2	0.2	⋯	⋯	⋯
V21	−15.1	13.9	0.1	⋯	⋯	⋯
V22	−20.7	−3.6	0.2	⋯	⋯	⋯
V23	−15.1	−11.7	0.7	2.6	3.2	7.9
	17.8	−5.2	1.5	2.5	1.3	3.1
	−19.2	17.1	0.8	2.2	2.7	5.2
V24	−5.5	9.9	0.4	⋯	⋯	2.5
V26	15.1	6.7	1.4	2.1	2.2	3.6
V28	−23.4	−28.5	0.9	1.4	1.7	1.9
V30	−0.0	−0.2	5.3	8.5	14.9	47.4
V31	−15.1	17.8	0.2	⋯	⋯	⋯
V32	8.3	8.5	1.8	5.2	8.7	25.6
V35	66.1	25.8	0.2	⋯	⋯	2.7
V36	31.6	−15.4	1.7	1.6	1.0	2.1
V37	20.5	60.9	0.9	0.6	0.5	⋯
V38	2.7	16.0	0.7	0.9	1.2	2.7
V39	2.8	10.5	0.9	1.9	2.1	2.3
V40	−9.6	−21.8	2.2	2.5	1.1	6.1
	6.9	11.7	2.0	2.2	2.7	18.3
V43	−6.9	−20.0	0.2	⋯	⋯	⋯
V46	8.2	4.9	0.1	⋯	⋯	⋯
	4.1	−39.0	0.3	1.8	⋯	⋯
V47	4.1	8.8	0.1	1.1	1.7	4.7
V49	−19.3	−24.1	0.4	0.8	⋯	⋯
V50	15.1	48.0	0.2	⋯	⋯	⋯

TABLE 5—*Continued*

BLAST ID	$\Delta\alpha^a$ ($''$)	$\Delta\delta^a$ ($''$)	$F_8.3$ (Jy)	$F_{12.1}$ (Jy)	$F_{14.7}$ (Jy)	$F_{21.3}$ (Jy)
V51	-2.8	-7.9	0.2	$\cdots$	$\cdots$	$\cdots$
V52	-4.1	0.0	0.2	$\cdots$	$\cdots$	3.3
V53	-20.7	-29.8	0.1	$\cdots$	$\cdots$	$\cdots$
V55	-17.9	11.8	0.2	$\cdots$	$\cdots$	$\cdots$
V57	-1.4	-11.7	1.3	1.3	1.2	1.2
V59	1.4	1.5	0.8	1.1	0.6	$\cdots$
V60	-52.2	5.7	0.1	1.0	$\cdots$	$\cdots$

NOTE.—All candidate *MSX* counterparts are listed for each BLAST source (§3.4).

[a]BLAST source tangent plane offsets (E and N) compared to *MSX* source position.

TABLE 6

RESULTS FROM SED FITS

BLAST ID	Temperature (K)	M_c ($M_\odot$)	L_{FIR} ($L_\odot$)	Luminosity Fraction (%)	L_{FIR}/M_c ($L_\odot\,M_\odot^{-1}$)
V01	27.2 ± 1.5	44 ± 7	750 ± 130	76	17.5 ± 5.0
V02	31.9 ± 2.3	114 ± 22	4500 ± 1000	78	40.5 ± 15.8
V03	22.2 ± 0.9	273 ± 40	1470 ± 150	67	5.6 ± 1.2
V04	20.0	38 ± 5	121 ± 15	$\cdots$	3.2
V05	31.3 ± 1.9	130 ± 27	4910 ± 880	89	36.1 ± 12.2
V06	20.2 ± 2.4	55 ± 35	96 ± 57	62	1.9 ± 1.9
V07	32.6 ± 1.9	579 ± 122	28200 ± 4900	83	49.0 ± 16.5
V08	29.7 ± 1.7	97 ± 19	2610 ± 430	84	26.5 ± 8.8
V09	22.8 ± 1.7	233 ± 45	1560 ± 350	80	6.4 ± 2.4
V10	15.8 ± 2.6	89 ± 50	53 ± 22	93	0.9 ± 0.9
V11	12.3 ± 1.6	213 ± 125	42 ± 15	$\cdots$	0.2 ± 0.1
V12	21.9 ± 1.0	42 ± 8	220 ± 30	51	5.3 ± 1.3
V13	16.5 ± 1.5	85 ± 28	87 ± 20	70	1.0 ± 0.5
V14	22.6 ± 1.0	17 ± 5	107 ± 11	70	6.0 ± 1.6
V15	17.8 ± 1.5	93 ± 23	145 ± 43	$\cdots$	1.5 ± 0.7
V16	20.2 ± 2.0	39 ± 16	117 ± 34	$\cdots$	2.9 ± 1.6
V17	19.0 ± 1.1	651 ± 171	1400 ± 280	$\cdots$	2.3 ± 0.8
V18	30.3 ± 1.5	148 ± 24	4590 ± 740	58	30.9 ± 9.3
V19	20.0	281 ± 67	890 ± 210	$\cdots$	3.2
V20	16.6 ± 3.1	1274 ± 739	1250 ± 590	75	0.9 ± 0.9
V21	15.8 ± 3.2	1109 ± 762	920 ± 540	66	0.9 ± 0.9
V22	17.7 ± 1.3	145 ± 34	227 ± 44	72	1.6 ± 0.6
V23	39.4 ± 1.7	526 ± 65	71000 ± 11000	89	130.4 ± 31.6
V24	23.2 ± 0.8	970 ± 121	6770 ± 640	68	6.7 ± 1.0
V25	17.6 ± 2.6	93 ± 44	112 ± 61	100	1.3 ± 1.1
V26	18.9 ± 1.1	150 ± 27	346 ± 62	58	2.4 ± 0.7
V27	14.9 ± 2.6	105 ± 64	54 ± 26	$\cdots$	0.6 ± 0.6
V28	15.9 ± 1.8	90 ± 46	60 ± 25	39	0.8 ± 0.7
V29	20.0	23 ± 4	73 ± 14	$\cdots$	3.2
V30	25.9 ± 1.0	680 ± 115	9020 ± 700	63	13.0 ± 2.9
V31	16.8 ± 1.7	43 ± 14	45 ± 22	50	1.0 ± 0.6
V32	26.2 ± 1.3	208 ± 30	2820 ± 410	69	13.7 ± 3.7
V33	14.2 ± 2.3	107 ± 64	49 ± 21	$\cdots$	0.4 ± 0.4
V34	20.0	52 ± 6	166 ± 18	$\cdots$	3.2
V35	20.7 ± 1.2	22 ± 7	84 ± 19	54	4.0 ± 1.1
V36	20.0	118 ± 12	374 ± 39	54	3.2
V37	22.6 ± 0.9	24 ± 6	139 ± 18	73	5.8 ± 1.5
V38	20.0	132 ± 13	417 ± 42	72	3.2
V39	21.7 ± 0.6	78 ± 8	390 ± 32	70	5.0 ± 0.7
V40	28.0 ± 1.6	142 ± 26	2670 ± 610	66	18.3 ± 6.9
V41	20.8 ± 0.8	110 ± 14	423 ± 43	$\cdots$	3.8 ± 0.8
V42	20.0	49 ± 6	155 ± 18	$\cdots$	3.2
V43	20.0	45 ± 5	142 ± 15	86	3.2
V44	18.3 ± 1.3	53 ± 15	103 ± 21	$\cdots$	2.0 ± 0.7

TABLE 6—*Continued*

BLAST ID	Temperature (K)	M_c (M$_\odot$)	L_{FIR} (L$_\odot$)	Luminosity Fraction (%)	L_{FIR}/M_c (L$_\odot$ M$_\odot^{-1}$)
V45	20.0	14 ± 4	46 ± 13	$\cdots$	3.2
V46	21.4 ± 1.7	37 ± 12	163 ± 35	66	4.5 ± 1.4
V47	20.2 ± 2.9	219 ± 70	830 ± 310	61	3.4 ± 2.3
V48	22.5 ± 1.7	25 ± 7	154 ± 34	$\cdots$	5.8 ± 2.3
V49	20.0	64 ± 6	203 ± 18	58	3.2
V50	21.1 ± 2.1	25 ± 10	101 ± 31	72	4.0 ± 2.4
V51	16.6 ± 3.4	1088 ± 727	1050 ± 570	70	1.2 ± 1.2
V52	24.6 ± 1.4	390 ± 75	3850 ± 610	84	9.7 ± 3.1
V53	18.5 ± 1.3	80 ± 17	156 ± 34	80	1.8 ± 0.7
V54	24.9 ± 1.3	210 ± 48	2320 ± 410	$\cdots$	10.5 ± 3.2
V55	20.0	48 ± 6	153 ± 17	59	3.2
V56	16.1 ± 1.3	180 ± 42	176 ± 49	$\cdots$	0.9 ± 0.5
V57	20.1 ± 1.1	58 ± 9	181 ± 31	60	3.1 ± 1.0
V58	16.7 ± 3.9	757 ± 510	540 ± 330	$\cdots$	0.8 ± 0.7
V59	25.4 ± 1.5	297 ± 67	3400 ± 390	63	12.2 ± 4.4
V60	15.8 ± 2.3	65 ± 28	42 ± 21	34	0.6 ± 0.5

NOTE.—Results from modified blackbody SED (Equation 4) fits to submillimeter and FIR photometry (§4). These fits assume a dust emissivity index $\beta = 1.5$. Cloud masses M_c are derived from the amplitude A of the SED using Equation 5 and distances from §5. FIR luminosities, L_{FIR}, are the integrated luminosities from the modified blackbody. Objects with MIR photometry have estimates for the total bolometric luminosity, which may be obtained by dividing the FIR luminosity by the Luminosity Fraction. Quoted uncertainties are statistical errors derived from Monte Carlo simulations (§4.2). Other systematic errors are not included. For example, adopting $\beta = 2.0$ decreases temperatures by $\sim 5\,$K, and increases cloud masses by a factor ~ 2 (§4.2). There are also significant distance uncertainties (§5), and a factor of ~ 2 uncertainty introduced through choices of κ_0 and R in Equation 5.